nature communications

Article

https://doi.org/10.1038/s41467-025-65312-y

Microbiome modulation uncouples efficacy and toxicity induced by immune checkpoint blockade in mouse multiple myeloma

Received: 26 December 2023

Accepted: 13 October 2025

Published online: 24 November 2025

Check for updates

Laura Lucia Cogrossi[1,2], Anna Policastro[1], Paola Zordan[1], Matteo Grioni[1], Anna Tosi[3], Nathalie Rizzo[4], Benedetta Mattorre[1], Marco Lorenzoni[1], Greta Meregalli[1], Sofia Sisti[2,5], Francesca Sanvito[4], Alessandro Palmioli[6,7], Cristina Airoldi[6], Aurora Maurizio[8], Marta Chesi[9], Leif Bergsagel[9], Nicola Clementi[2,5], Antonio Rosato[3,10] & Matteo Bellone[1]

Smoldering multiple myeloma (SMM), which is in principle curable, may develop into life-threatening MM. Intestinal microbiota and gut-born T helper-17 (Th17) lymphocytes may contribute to this development, but the mechanisms are unclear. Here we demonstrate that administering the human commensal *Prevotella melaninogenica* to transgenic Vk*MYC mice that exhibit SMM-like phenotypes delays the evolution to full-blown MM. Mechanistically, *P. melaninogenica* increases the production of short-chain fatty acids (SCFA), thereby preventing the skewing of dendritic cells towards a pro-Th17 phenotype and subsequently accumulation of Th17 cells in the bone marrow of treated mice. *P. melaninogenica* or butyrate synergizes with anti-PD-L1 or anti-TIGIT to suppress myeloma progression by restraining Th17 cell expansion while inducing effector $CD8^+$ T cells. *P. melaninogenica* also attenuates IL-17-mediated skin lesions that mimic anti-PD-L1-induced adverse events. Our results thus suggest that gut microbiota modulation or SCFAs administration may represent treatment options for patients affected by plasma cell dyscrasias.

Multiple myeloma (MM) is a treatable but incurable B-cell neoplasm characterized by the accumulation of clonal plasma cells within the bone marrow (BM), anemia, hypercalcemia, renal insufficiency, and bone lesions. MM accounts for 1% of all cancers and approximately 10–15% of all hematological malignancies[1]. Asymptomatic smoldering MM (SMM), which occurs in approximately 0.5% of the population above 40 years and is in principle curable, may anticipate MM[2]. Likely because SMM is a heterogeneous disease and its pathobiology is poorly understood, treatment is restricted to a few high-risk patients, whereas active surveillance is recommended to all the others[2]. Considering that SMM has an overall risk of progression to MM at 10% per year[2], active surveillance leaves many SMM patients in anxiety and frustration.

The intestinal microbiota may represent one tumor cell-extrinsic mechanism driving SMM-to-MM transition[3]. In transgenic Vk*MYC mice developing de novo MM[4], the human, Gram-negative commensal *Prevotella heparinolytica* promoted the differentiation of gut-born Th17 cells that migrated to the BM, where they favored neoplastic

[1]Cellular immunology Unit, Division of Immunology, Transplantation and Infectious Diseases, IRCCS Ospedale San Raffaele, Milan, Italy. [2]Vita-Salute San Raffaele University, Milan, Italy. [3]Immunology and Molecular Oncology Diagnostics, Istituto Oncologico, Veneto Padua, Italy. [4]Pathology and histology department, IRCCS Ospedale San Raffaele, Milan, Italy. [5]Laboratory of Microbiology, IRCCS Ospedale San Raffaele, Milan, Italy. [6]Università degli studi Milano-Bicocca, Milan, Italy. [7]BioOrg NMR Lab, Department of Biotechnology and Biosciences, University of Milano-Bicocca, Milan, Italy. [8]Center for Omics Sciences, IRCCS San Raffaele Scientific Institute, Milan, Italy. [9]Mayo Clinic, Scottsdale, Arizona, USA. [10]Department of Surgery, Oncology and Gastroenterology (DiSCOG), University of Padua, Padua, Italy. e-mail: bellone.matteo@hsr.it

plasma cell expansion, and evolution from an asymptomatic disease mimicking SMM (i.e., Early MM; ref. 5) to symptomatic MM (Late-MM; ref. 6). Conversely, *P. melaninogenica*, which correlates with better prognosis in humans affected by autoimmune diseases[7], restrained Th17 cell expansion and prolonged animal survival. Mechanistically, IL-17 induced STAT3 phosphorylation in neoplastic plasma cells and activated eosinophils. Blocking the IL-17 pathway delayed disease progression in Vk*MYC mice[6]. Similarly, in MM patients affected by SMM, higher levels of BM IL-17 predicted faster disease progression[6]. Altogether, these premises suggest that microbiota modulation would represent a safe SMM treatment.

The intestinal microbiome has also gained momentum in the context of cancer immunotherapy, and, because the gut microbiota can empower immune checkpoint blockade (ICB)[8] clinical trials of oral supplementation with probiotics in combination to ICB are ongoing (NCT03358511, NCT03829111, NCT05032014, NCT05094167, NCT05865730).

T cells in MM patients express PD-1 and are functionally exhausted/senescent[9], and PD-1-expressing T cells are enriched in the BM of SMM patients who progressed to active MM[10]. ICB targeting PD-1/PD-L1 have been tested in MM, also supported by the evidence that PD-L1 is selectively expressed on neoplastic plasma cells[11]. PD-L1 may also act on plasma cells as an oncogenic protein, and its expression correlates with disease progression and relapse[12]. However, all trials combining anti-PD-1/PD-L1 antibodies, dexamethasone and immune modulatory drugs in MM were halted by the US FDA because of an unfavorable benefit-risk profile and life-threatening immune-related adverse events (IrAEs)[11].

Since specific microbiota signatures have been associated with IrAEs[13,14], which are often induced by IL-17-producing cells[15], we hypothesized that administering probiotics could be a valid strategy to limit these adverse events while simultaneously improving anti-tumor immunity.

We challenged this hypothesis in Vk*MYC mice and show that modulation of the gut microbiota is a disease-modifying treatment per se. In addition, when given in combination with anti-PD-L1 or anti-TIGIT antibodies, *P. melaninogenica* substantially modifies the trajectory of SMM-to-MM progression. More importantly, it also limits ICB-related skin toxicity. Our findings justify testing probiotics, both alone and with ICB, to maximize their antitumor effects in plasma cell dyscrasias and other cancers where Th17 cells are a driving force.

Results

P. melaninogenica delays progression from Early- to Late-MM

To investigate the effect of *P. melaninogenica* on SMM-to-MM progression, we set up a preclinical trial enrolling individual Vk*MYC mice when they reached the phase of asymptomatic Early-MM [i.e., measurable M-spike < 6% which corresponds to gamma/albumin ratios ranging between 0.15 and 0.4 (Supplementary Fig. 1a; ref. 5). Median age at inclusion 40 weeks]. This model is relevant because Early-MM mice, if left untreated, invariably evolve to symptomatic Late-MM, thus mimicking, also for age, those 10% SMM patients that each year progress to MM[2]. Mice were screened and randomly assigned to either treatment, as for clinical trials involving humans. Male and female mice were randomly included in the study to investigate potential sex-related bias. Ten months were required to enroll all the mice, and the entire experiment lasted 26 months (Supplementary Data 1). This extended time frame ensured sufficient genetic variability from secondary mutations[16], enhanced reproducibility, and allowed for the identification of potential outliers end errors. At enrollment, all mice displayed similar levels of M-spike (i.e., gamma globulins/albumin ratio; Supplementary Fig. 1b) and normal hemoglobin levels (Fig. Supplementary Fig. 1c). To favor acceptance of the commensal, mice received broad spectrum antibiotics in the week before being randomly assigned to either receive *P. melaninogenica* or vehicle (PBS; Fig. 1a). Mice reached Late-MM when their M-spike was ≥6% (i.e., gamma/albumin ratio ranging between 0.35 and 0.75; Supplementary Fig. 1a; ref. 5). Hemoglobin drop was also taken as indication of Late-MM[5] (Fig. 1b and c). At week 10, M-spike levels in *P. melaninogenica*-treated mice were halved compared to PBS-treated mice (Fig. 1d). By week 14, 50% of mice in the *P. melaninogenica*-treated group evolved to Late-MM compared to 90% in the PBS group, and overall progression to advanced MM was delayed by *P. melaninogenica* (Fig. 1e). Thus, modulating the gut microbiota was sufficient to delay disease evolution in Early-MM mice.

Because the gut microbiota also contributes to ICB efficacy[8] and neoplastic plasma cells both in humans[17] and in Early-MM mice express PD-L1 (Fig. 1f), we treated Early-MM mice with anti-PD-L1 antibodies alone or in combination with *P. melaninogenica*. Early-MM mice treated with anti-PD-L1 experienced delayed progression to Late-MM (Fig. 1d, e). Addition of *P. melaninogenica* to anti-PD-L1 further delayed disease evolution (Fig. 1d, e) and, when all Vk*MYC mice in the control group had evolved to Late-MM, more than 60% of the mice receiving the combined treatment were still in the Early-MM phase (Fig. 1e). At the end of the observation period, 20% of mice in the combination group had not evolved to MM (Fig. 1e). We did not notice any substantial difference in response to *P. melaninogenica*, anti-PD-L1 or their combination between male and female mice (Supplementary Fig. 1d–g). In addition, most of the mice receiving the combined treatment experienced limited hemoglobin drop (Fig. 1b), as confirmed by the comparison of the area under the curve (AUC) between this and the PBS group (Fig. 1c). Thus, *P. melaninogenica* and ICB synergize in delaying evolution to incurable MM.

To perform a controlled study on genetically homogeneous tumors, mice exposed to *P. melaninogenica* were challenged with Vk12598 cells (t-VkMYC; Fig. 1g). This model mimics bortezomib-resistant MM and has been used to successfully predict therapeutic efficacy in humans[18]. *P. melaninogenica* given as a single treatment limited disease appearance (Supplementary Fg. 1h) and anemia (Fig. 1h) and prolonged survival of t-VkMYC mice (Fig. 1i). Our experimental setup required broad-spectrum antibiotics before *P. melaninogenica* supplementation because the beneficial effect of *P. melaninogenica* was lost in mice not receiving antibiotics (Supplementary Fig. 1i, j). Treatment with anti-PD-L1 antibodies (Fig. 1g–i and Supplementary Fig. 1h) but not control IgG (Supplementary Fig. 1k) exerted effects overlapping *P. melaninogenica*. Importantly, the combination of *P. melaninogenica* and anti-PD-L1 provided additional survival advantage (Fig. 1i) and further contained anemia (Fig. 1h). t-VkMYC mice treated with the Gram-positive skin commensal, *Staphylococcus epidermidis*, developed MM with kinetics similar to vehicle-treated mice. Furthermore, gavage with *S. epidermidis* did not alter the disease course when combined with ICB (Supplementary Fig. 1l). Thus, only *P. melaninogenica* and ICB synergize in limiting disease aggressiveness in t-VkMYC mice.

P. melaninogenica curbs Th17 cells and unleashes ICB-induced T cells

Because IL-17 has been associated with faster SMM-to-MM progression, and in Vk*MYC mice, treatment with *P. melaninogenica* restrains Th17 cell expansion and prolongs animal survival[6], we quantified IL-17-producing cells in the intestine, spleen (SPL) and BM of treated Vk*MYC mice (Supplementary Data 2). Organs were collected when mice reached Late-MM (i.e., M-spike > 6%), except for one mouse in the P. *melaninogenica* + anti-PD-L1 group that was euthanized at the end of the observation period. Except for the latter mouse in the combined treatment group (black dot; supplementary Fig. 1m), most of the mice were euthanized at similar levels of M-spike (Supplementary Fig. 1m), which is indicative of BM infiltration by neoplastic plasma cells[5]. Despite comparable tumor burden and $CD4^+$ T cells in Peyer's patches (PPs), BM and spleen of mice receiving either treatment

https://doi.org/10.1038/s41467-025-65312-y

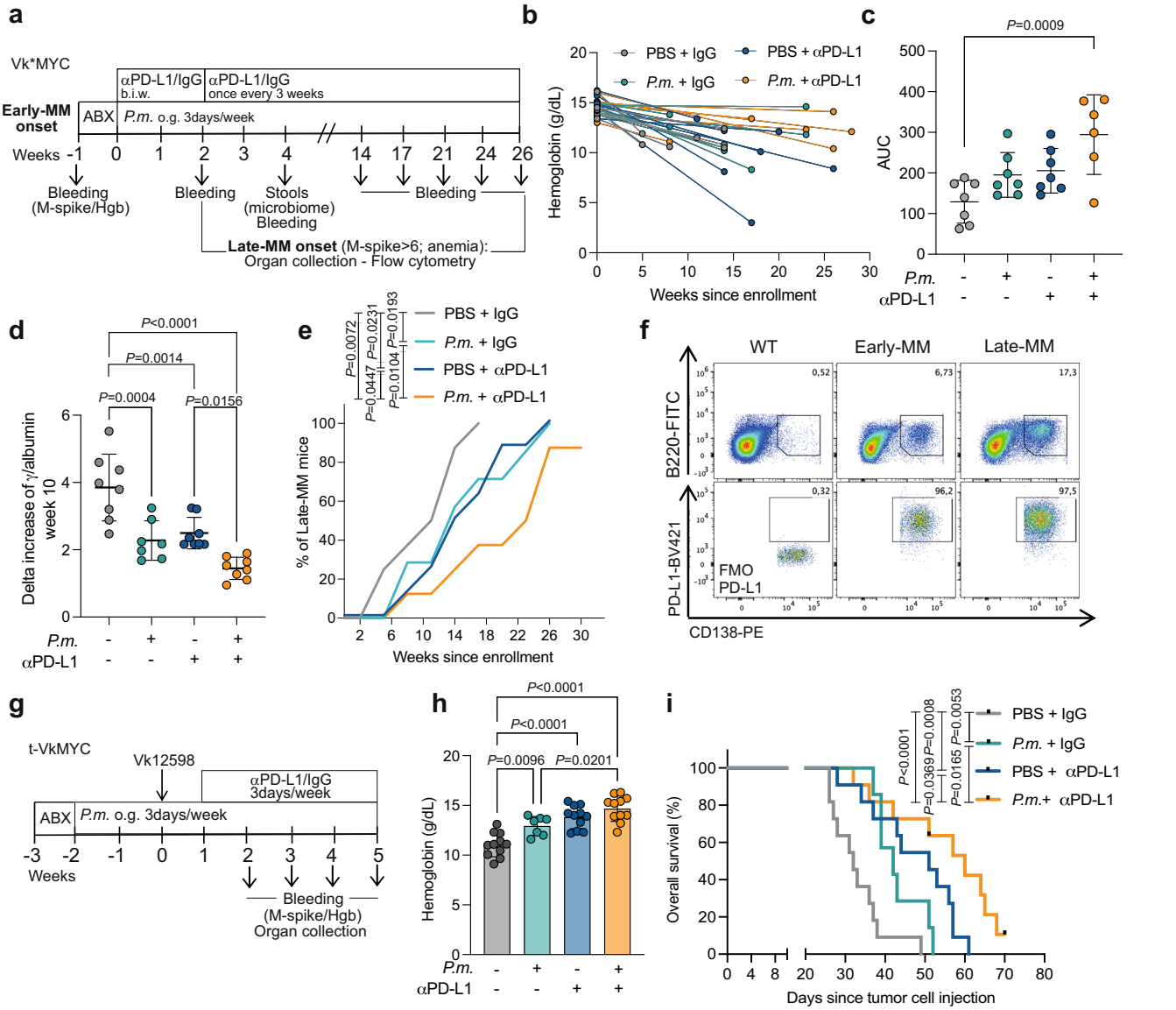

Fig. 1 | Combination of probiotic *P. melaninogenica* and anti-PD-L1 in Early-MM mice delays progression to Late-MM and prolongs survival in bortezomib-resistant MM. **a** Treatment schedule for experiments **b**–**e**: Each single Vk*MYC mouse was enrolled at Early-MM onset and treated individually, mimicking a human clinical trial. After one week of antibiotics (ABX) mice were randomly assigned to the following treatments: Vehicle (PBS) + Isotype control (IgG): PBS + anti-(α)PD-L1; *P.m.* + IgG; *P.m.* + αPD-L1. Both male and female mice were included in each experimental group. M-spike levels and hemoglobin (Hgb) were measured in the peripheral blood (Bleeding) to determine Late-MM progression. **b**, **c** Hemoglobin quantification (**b**) and area under the curve (**c**) of mice at enrollment and at the time of Late-MM progression. PBS + IgG $n = 7$; *P.m.*+ IgG $n = 7$; PBS + αPD-L1 $n = 7$; *P.m.* + αPD-L1 $n = 6$. Each dot represents one mouse. Data are presented as mean ± SD. Statistical analysis by One-Way ANOVA. **d** Delta increase of γ/albumin ratio for each mouse 10 weeks after enrollment. PBS + IgG $n = 8$; *P.m.* + IgG $n = 7$; PBS + αPD-L1 $n = 8$; *P.m.*+ αPD-L1 $n = 8$. Each dot represents one mouse. Data are presented as mean ± SD. Statistical analysis by One-Way ANOVA. **e** Percentage of Early-MM Vk*MYC mice progressing to Late-MM overtime. One-way ANOVA. PBS + IgG $n = 8$; *P.m.*+ IgG $n = 7$; PBS + αPD-L1 $n = 8$; *P.m.* + αPD-L1 $n = 8$. **f** Representative flow cytometry plots of PD-L1 expression gated on BM plasma cells (identified as $B220^{-}CD138^{+}$ cells in $CD45^{+}$ cells) from WT, Early-MM, Late-MM mice. **g** Treatment schedule for female C57BL/6 mice injected with Vk12598 MM cells (t-VkMYC) conditioned with *P.m.* or vehicle (PBS) and receiving αPD-L1 or IgG. M-spike levels and anemia were measured weekly in the peripheral blood. **h** Hemoglobin quantification from mice treated as in g, four weeks after tumor injection. PBS+IgG $n = 11$, *P.m.*+IgG $n = 7$, PBS + αPD-L1 $n = 11$, *P.m.* + αPD-L1 $n = 11$. Data are presented as mean ± SD. Each dot represents one mouse. One-Way ANOVA. **i** Overall survival of female t-VkMYC mice described in g. PBS + IgG $n = 11$, *P.m.*+ IgG $n = 7$, PBS + αPD-L1 $n = 11$, *P.m.*+ αPD-L1 $n = 11$. Log-rank (Mantel–Cox) test. Data in panels (**h** and **i**) are pooled from three independent experiments. Source data are provided as a Source Data file.

(Supplementary Fig. 2a–d), Th17 cells were less represented in the PPs (Fig. 2a, b and Supplementary Fig. 2e) and in the BM of *P. melaninogenica*-treated mice (Fig. 2c, d and Supplementary Fig. 2f), while in the spleen of the same animals, we measured a trend towards Th17 cell reduction (Supplementary Fig. 2g and h). Strikingly, this was also true for mice exposed to the combined treatment (Fig. 2a–d and Supplementary Fig. 2e–h). Similar results were obtained in t-VkMYC mice exposed to single or combined treatments (Supplementary Fig. 2i–m). t-VkMYC mice were euthanized at similar M-spike levels between week 3 and 6 after tumor cell injection (Supplementary Fig. 2n, o). Hence, *P. melaninogenica* contains disease-induced expansion of Th17 cells even under ICB treatment. Consistently with disease aggressiveness in t-VkMYC mice (Supplementary Fig. 1l), *S. epidermidis* did not alter the proportion of Th17 cells in the PPs (Supplementary Fig. 2l) and in the BM (Supplementary Fig. 2m) supporting the specificity of *P. melaninogenica* immunomodulation.

https://doi.org/10.1038/s41467-025-65312-y

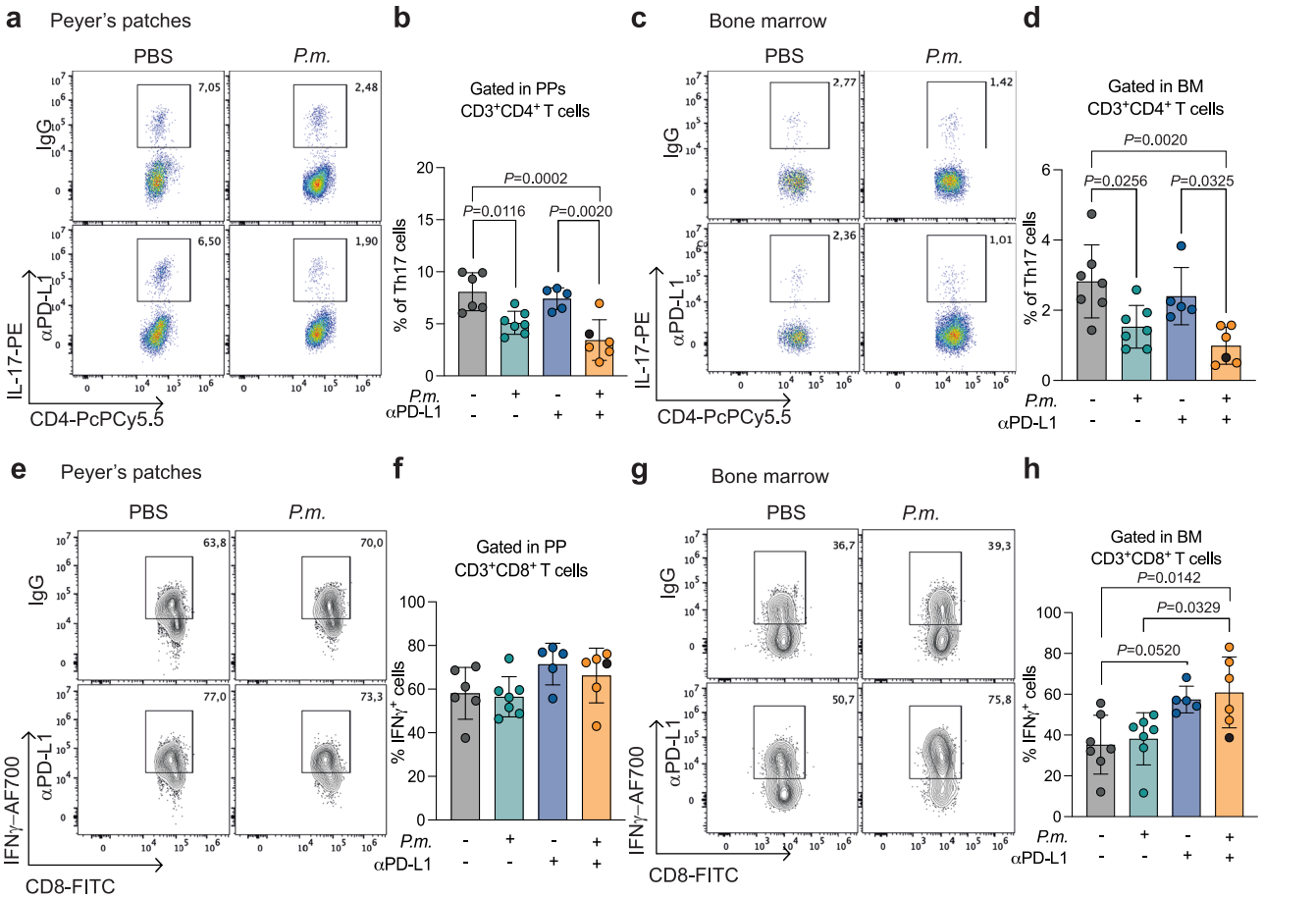

Fig. 2 | *P. melaninogenica* limits Th17 cell expansion fully unleashing the cytotoxic response elicited by anti-PD-L1. a, **b** Representative flow cytometry plots (**a**) and quantification (**b**) of IL-17 producing cells gated in $CD3^+CD4^+$ T cells (Th17 cells) in the PPs of animals described in Fig. 1a–e. **c**, **d**. Representative flow cytometry plots (**c**) and quantification (**d**) of Th17 cells in the BM of the same animals. **e, f** Representative flow cytometry plots (**e**) and quantification (**f**) of IFNγ production gated in $CD3^+CD8^+$ T cells in the PPs of animals described in Fig. 1a–e. **g, h**. Representative flow cytometry plots (**g**) and quantification (**h**) for IFNγ production gated in $CD3^+CD8^+$ T cells in the BM of the same animals. Representative gating strategy is reported in Supplementary Fig. 2. Panels **b, f**: PBS+IgG $n = 6$; *P.m.*+IgG $n = 7$; PBS + αPD-L1 $n = 5$; *P.m.*+αPD-L1 $n = 6$; Panels **d, h**: PBS+IgG $n = 7$; *P.m.*+IgG $n = 7$; PBS + αPD-L1 $n = 5$; *P.m.*+αPD-L1 $n = 6$. Each dot represents one mouse. Black dot indicates Early-MM mouse euthanized at the end of observational period. Data are presented as mean ± SD. Statistical analysis by One-Way ANOVA. Source data are provided as a Source Data file.

ICB is expected to rejuvenate CD8-mediated anti-tumor immunity[9]. Indeed, while $CD8^+$ T cells in the PPs were not affected by treatments (Fig. 2e, f), much more IFNγ-producing $CD8^+$ T cells infiltrated the BM and the spleen of mice treated with ICB (Fig. 2g, h and Supplementary Fig. 3a–c) and in the BM tended to express lower levels of PD-1 molecule compared to IgG treatment (Supplementary Fig. 3d–f). A trend towards expansion of IFNγ-producing CD8 T cells in the PPs of mice treated with ICB and *P. melaninogenica* (Fig. 2e, f) was not confirmed by absolute numbers (Supplementary Fig. 3g). The potent CD8-mediated immune response induced by ICB in the BM was maintained in mice also treated with *P. melaninogenica* (Fig. 2e, h), showing that the effect of *P. melaninogenica* substantially and persistently extends beyond the intestinal tract to the BM, where it reduces the expansion of pathogenic Th17 cells without dampening the antitumor response elicited by anti-PD-L1. Similarly, anti-PD-L1-induced expansion of $IFN\gamma^+$ CD8 T cells in the BM and SPL of t-VkMYC mice was not reduced by the addition of *P. melaninogenica* (Supplementary Fig. 3h–j). Also, treatment with *S. epidermidis* combined with anti-PD-L1 did not provide further immunological advantage to anti-PD-L1-treated mice (Supplementary Fig. 3k–m).

P. melaninogenica restrains IL-17-mediated skin toxicity

Severe IrAEs in patients receiving ICB in combination with immunomodulatory drugs[11] precluded further clinical investigation. The microbiota affects IrAEs, especially in the gastrointestinal tract and the skin[13] and IL-17 blocking antibodies can treat ICB-induced psoriasis[15]. Having provided evidence that *P. melaninogenica* contains Th17 cell expansion even under ICB, we asked if it also restrains IL-17 and IL-17-producing cells that ignite dermatological toxicity[15]. Because anti-PD-L1 alone does not induce skin toxicity in our models, we applied imiquimod to anti-PD-L1-treated mice to model ICB-induced psoriasis-like lesions (Supplementary data 3). Imiquimod-induced skin reaction is mediated by IL-17[19] and the inhibition of PD-1 signaling in mice enhances IL-17-mediated psoriatic dermatitis[20]. Similarly, ICB aggravated imiquimod-induced psoriasis-like lesions (Supplementary Fig. 4a) and increased the immune cell infiltrate (mIHC; Supplementary Fig. 4b–e). Mice receiving *P. melaninogenica* in addition to imiquimod/anti-PD-L1 treatment showed moderated skin pathology (Fig. 3a) with significantly reduced hyperkeratosis (Fig. 3b), and a trend toward reduced severity grade of acanthosis (Fig. 3c) and inflammatory infiltration (Fig. 3d). Treatment with *P. heparinolytica* did not significantly impact the severity of skin lesions induced by imiquimod/anti-PD-L1 treatment (Fig. 3b–d). mIHC (Fig. 3e–i) showed significantly reduced gut-born (i.e., $\alpha4\beta7^+$) cells in the skin of Imiquimod/anti-PD-L1-treated mice receiving *P. melaninogenica* compared to vehicle- or *P. heparinolytica*-treated mice (Fig. 3f), suggesting restrained migration of immune cells from the gut into the skin of *P. melaninogenica*-treaded mice. Total $CD11c^+$ cells (Fig. 3g), and $\alpha4\beta7^+CD11c^+$ cells

https://doi.org/10.1038/s41467-025-65312-y

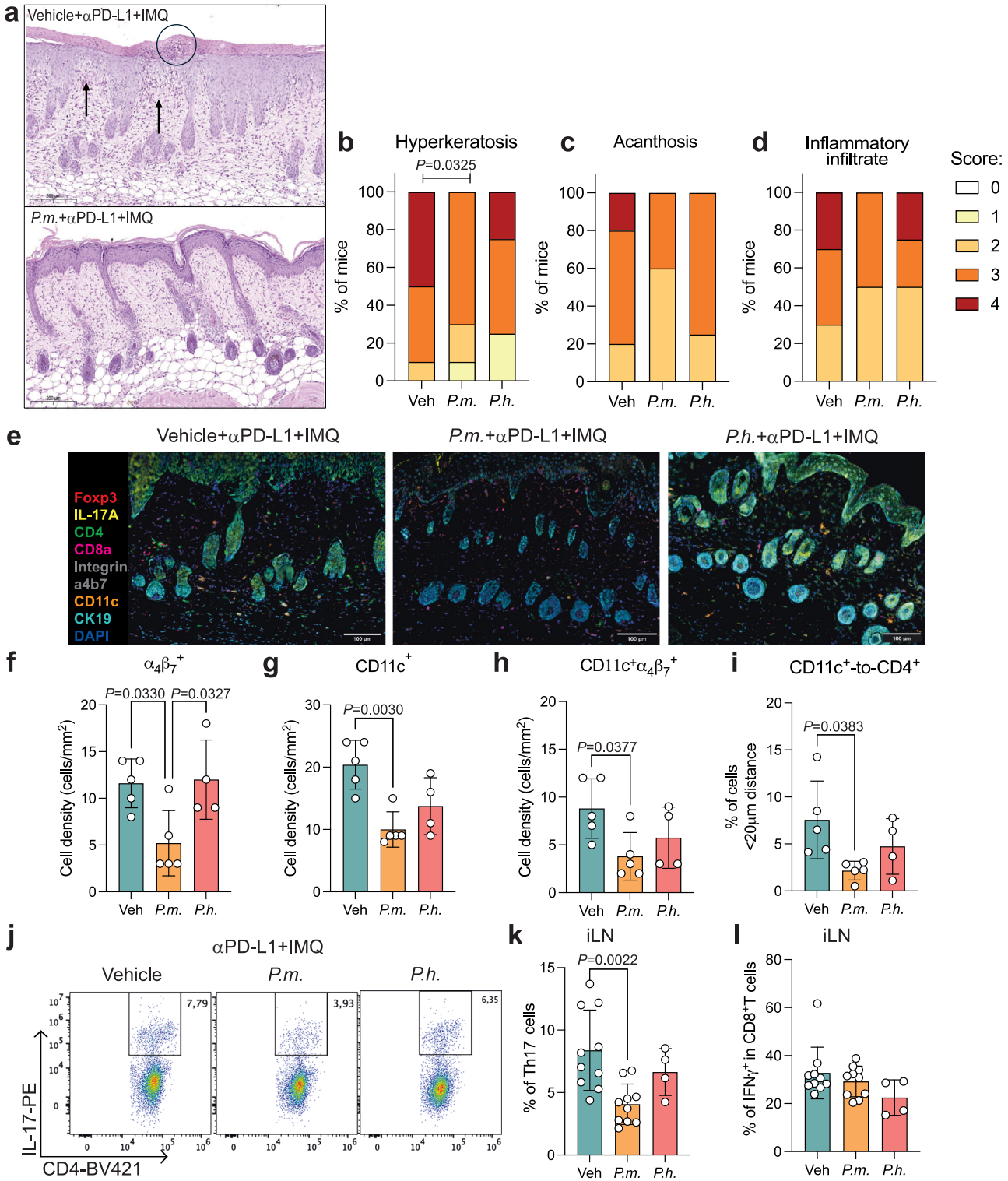

Fig. 3 | *P. melaninogenica* restrains IL-17-mediated dermatological toxicity upon ICB treatment. a Representative images of skin histopathology (H&E staining) from female mice treated with imiquimod (IMQ) + αPD-L1 in the absence (left) or presence (right) of *P.m.* Magnification 15X. Arrow indicates spongiosis, circle indicates microabscess. **b**–**d** Stacked bar plot showing the percentage of mice according to the histopathological score for hyperkeratosis (**b**), acanthosis (**c**), and inflammatory infiltrate (**d**). Mice were treated with IMQ and αPD-L1in the presence or not of indicated microbiota modulation with Vehicle $n = 10$, *P.m.* $n = 10$, or *P.h.* $n = 8$ mice/group. Scoring performed on 2 H&E stained slides of skin for each mouse. Statistical analysis by Fisher's test. **e** Representative multiplex IHC images from mice treated with IMQ + αPD-L1 with bacterial administration. Magnification 20X. **f**, **h** Cell density per slide of Integrin α4β7$^+$ cells (**f**), CD11c$^+$ cells (**g**) and α4β7$^+$CD11c$^+$ cells (**h**). Vehicle $n = 5$, *P.m.* $n = 5$, or *P.h.* $n = 4$ mice/group. Data are presented as mean ± SD. Each dot represents one mouse. Statistical analysis by One-way Anova. Data representative of two independent experiments. **i** Percentage of CD11c$^+$-CD4$^+$ cells at <20 µm distance. Vehicle $n = 5$, *P.m.* $n = 5$, or *P.h.* $n = 4$ mice/group. Each dot represents one mouse. Data are presented as mean ± SD. Statistical analysis by One-way Anova. Data representative of two independent experiments. **j**–**l** flow cytometry staining on the skin-draining lymph nodes (inguinal; iLN) of the same mice (**j**). Data show the percentage of Th17 cells (**k**) and IFNγ$^+$ cells gated in CD8$^+$ T cells (**l**). Veh: $n = 10$; *P.m.* $n = 10$; *P.h.* $n = 4$. Each dot represents one mouse. Statistical analysis by One-way Anova. Data are presented as mean ± SD. Source data are provided as a Source Data file.

(Fig. 3h), were also less represented and more distant from CD4⁺ T cells in *P. melaninogenica*-treated mice (Fig. 3i), suggesting that *P. melaninogenica* also impacts antigen presenting cell (APC) migration and function. While anti-PD-L1 administration did not modulate the frequency of IL-17⁺ cells infiltrating the skin of imiquimod-treated mice (Supplementary Fig. 4f) and the addition of *P. melaninogenica* only marginally reduced such infiltrate (Supplementary Fig. 4g), Th17 cells accumulated in skin-draining lymph nodes of treated mice (Supplementary Fig. 4h and i) and were only restrained by *P. melaninogenica* (Fig. 3j, k). IFNγ-producing cells remained unaltered (Fig. 3l). Thus, *P. melaninogenica* helps control or reduce skin toxicity by inhibiting the IL-17 pathway.

We also assessed the efficacy of *P. melaninogenica* in restraining IrAEs in the t-VkMYC model (Supplementary data 4). To better synchronize the evaluation of the skin, mice were euthanized five weeks after tumor injection and seven days after imiquimod application (Supplementary Fig. 4j). In this study, M-spike levels at sacrifice are detailed in Supplementary Fig. 4k. The data shows that *P. melaninogenica* treatment tended to reduce cutaneous inflammation and immune cell infiltration in the skin-draining lymph nodes (Supplementary Fig. 4l and m). Thus, *P. melaninogenica* uncouples the efficacy and toxicity of ICB.

P. melaninogenica modulates DC function to curb Th17 cells

Having found reduced α4β7⁺ in the skin of mice treated with *P. melaninogenica* (Fig. 3h), we asked if α4β7⁺ cells were also less represented in the BM of t-VkMYC mice treated with this commensal. In tumor-bearing mice, irrespective of the treatment, up to 10% CD45⁺ BM cells expressed the gut-homing marker α4β7 (Supplementary Fig. 5a, b). This fraction dropped to approximately 5% in the absence of a quantifiable M-spike (Supplementary Fig. 5b). We also found a comparable frequency of α4β7⁺ cells in the intestinal-draining lymph nodes (mLN) and the spleen of the same animals (Supplementary Fig. 5c, d), suggesting that BM accumulation of gut-derived immune cells is driven by inflammatory cues induced by the tumor. Because different subsets of mononuclear phagocytes (CD11b⁺ and/or CD11c⁺ cells) accounted for most gut-derived immune cells in the BM of t-VkMYC mice (Supplementary Fig. 5e) and microbiota conditioning by *P. melaninogenica* associated with reduced skin and iLN-infiltrating CD11c⁺ cells (Fig. 3g, h and supplementary Fig. 4l), we focused on dendritic cells (DCs). We compared the activity of the two *Prevotella* species on DCs because in vivo they exert distinct effects on Th17 cell induction (Fig. 3j, k and ref. 6). Upon treatment of t-VkMYC mice with either one of the two *Prevotella* strains (Supplementary Fig. 6a), less Th17 cells (Fig. 4a) and less DCs producing IL-6 and IL-1β (Fig. 4b and Supplementary Fig. 6b) were found in the BM of mice receiving *P. melaninogenica* compared to *P. heparinolytica*. Notably, *Prevotellae* administration did not alter the antigen-presenting capacity of these DCs (Supplementary Fig. 6c, d). IL-6 and IL-1β, together with IL-23, are involved in the differentiation of naïve T cells towards Th17 cells[21], and the amount of IL-6 increases in the BM of Vk*MYC mice, where it synergizes with IL-17 to promote neoplastic plasma cell survival[6]. Indeed, less DCs generated from BM precursors of WT mice (Supplementary Fig. 6f) produced IL-1β (Fig. 4c) when conditioned with *P. melaninogenica*, and skewed less naïve OTII cells[22] towards Th17 (Fig. 4d and Supplementary Fig. 6g) under suboptimal Th17-polarizing conditions (low-dose TGF-β and IL-6). These data suggest that *P. melaninogenica*-stimulated DCs provide insufficient inflammatory signals, including IL-1β, to drive optimal Th17 differentiation. Similarly, less human monocyte derived DCs (hMoDCs; Supplementary Fig. 6h) producing cytokines were found in *P. melaninogenica*-conditioned samples (Fig. 4e), and less naïve T cells became Th17 cells in the presence of *P. melaninogenica*-conditioned hMoDCs than *P. heparinolytica*-conditioned DCs (Fig. 4f and Supplementary Fig. 6i).

To gain mechanistic insights into the effects of *P. melaninogenica* on DCs, we performed RNA-seq on BMDCs cultured either with *P. melaninogenica* or *P. heparinolytica* (Fig. 4c). As depicted in Fig. 4g and Supplementary Fig. 7, P. *melaninogenica*-stimulated DCs expressed fewer genes associated with cytokine production and cytokine-mediated signaling pathways (e.g., *Cxcl9, Cxcl10, Il1b, Il6, Il12b)* as well as T cell proliferation (e.g., *Ccl5, Itgal, Cd40*), thus confirming flow cytometry functional assays (Fig. 4c–f). Conversely, *P. melaninogenica*-stimulated DCs upregulated genes belonging to sterol metabolism pathways (e.g., *Sqle, Cyp51, Msmo1*; Fig. 4h and Supplementary Fig. 7a, c) associated with homeostatic in vivo DCs maturation[23]. Thus, *P. melaninogenica* acts on DCs to curb the expansion of Th17 cells.

P. melaninogenica favors the production of SCFAs

Prevotella species produce short-chain fatty acids (SCFAs) from the fermentation of dietary fibers[24,25]. SCFAs act on epithelial and immune cells as histone deacetylase inhibitors to reduce IL-17, TNFα and IL-6 production[26]. Interestingly, stool samples from mice treated with *P. melaninogenica* contained more acetate, butyrate and tended to be richer in propionate than samples from *P. heparinolytica*-treated mice (Fig. 5a–c). While NMR-based metabolomic analysis of supernatants from *P. melaninogenica* cultures did not retrieve butyrate (Supplementary Fig. 8a), it showed abundance of acetate and succinate (Fig. 5d), the latter acting as precursor for butyrate production by certain Firmicutes bacteria[27]. Consistent with this, stools of *P. melaninogenica*-treated mice had low succinate levels (Fig. 5e), and a microbiota composition distinct from vehicle-treated mice (Supplementary Fig. 8b–e), with increased representation of the butyrate-producing *Lachnospiraceae*[28] (Fig. 5f). Thus, *P. melaninogenica* modulates the gut microbiota in favor of SCFA producers.

Butyrate restrains Th17 expansion and delays MM progression

SCFA-producing bacteria associate with beneficial outcomes in MM[25,29] and potentiate ICB[30,31]. Indeed, administration of either butyrate or acetate to t-VkMYC mice significantly prolonged their survival (Fig. 6a, b). The BM of butyrate-treated mice euthanized at similar M-spike levels (supplementary Fig. 9a) contained less DCs producing IL-6 (Fig. 6c) and IL-1β (Fig. 6d) and less Th17 cells (Fig. 6e) than mice treated with vehicle. Acetate reduced BM IL-6⁺ DCs (Fig. 6f) without affecting Th17 cell proportion (Fig. 6g). Instead, a significant expansion of IFNγ-producing CD4⁺ T cells in the latter (Fig. 6h) supported the hypothesis of a potent effector response induced by acetate[32]. When combined with ICB, only butyrate potentiated the antitumor effects of ICB (Fig. 6i–k and Supplementary Fig. 9b). Thus, only butyrate fully recapitulates the in vivo effects of *P. melaninogenica* (Figs. 1i, 2b, f and Supplementary Figs. 1h, 2i, 3h). In vitro, only butyrate limited LPS-induced DC maturation (Fig. 6l) without impairing their viability (Supplementary Fig. 9c). Whereas T cell viability and proliferation were also not impacted by SCFAs (Supplementary Fig. 9d–f), butyrate restrained Th17 cell differentiation (Fig. 6m). Consistently, butyrate administration to t-VkMYC mice lacking IL-17 (IL-17KO mice) failed to improve mouse survival (Fig. 6n and Supplementary Fig. 9g). Taken together, these data demonstrate that increased butyrate availability limits tumor aggressiveness by modulating IL-17-producing cells.

P. melaninogenica also improves efficacy of anti-TIGIT therapy

To further support the clinical applicability of our findings, we also assessed the therapeutic efficacy of *P. melaninogenica* in combination with ICB against TIGIT (Fig. 7a), a novel, promising target for MM therapy[33]. Anti-TIGIT monotherapy was well tolerated by all t-VkMYC mice (Fig. 7b) and significantly delayed tumor onset (Fig. 7c). The addition of *P. melaninogenica* to anti-TIGIT antibody treatment further prolonged disease-free survival in these mice (Fig. 7c). Treated animals also experienced a prolonged OS (Fig. 7d). Collectively, these findings support the clinical relevance of combining *P. melaninogenica* with ICB in MM.

https://doi.org/10.1038/s41467-025-65312-y

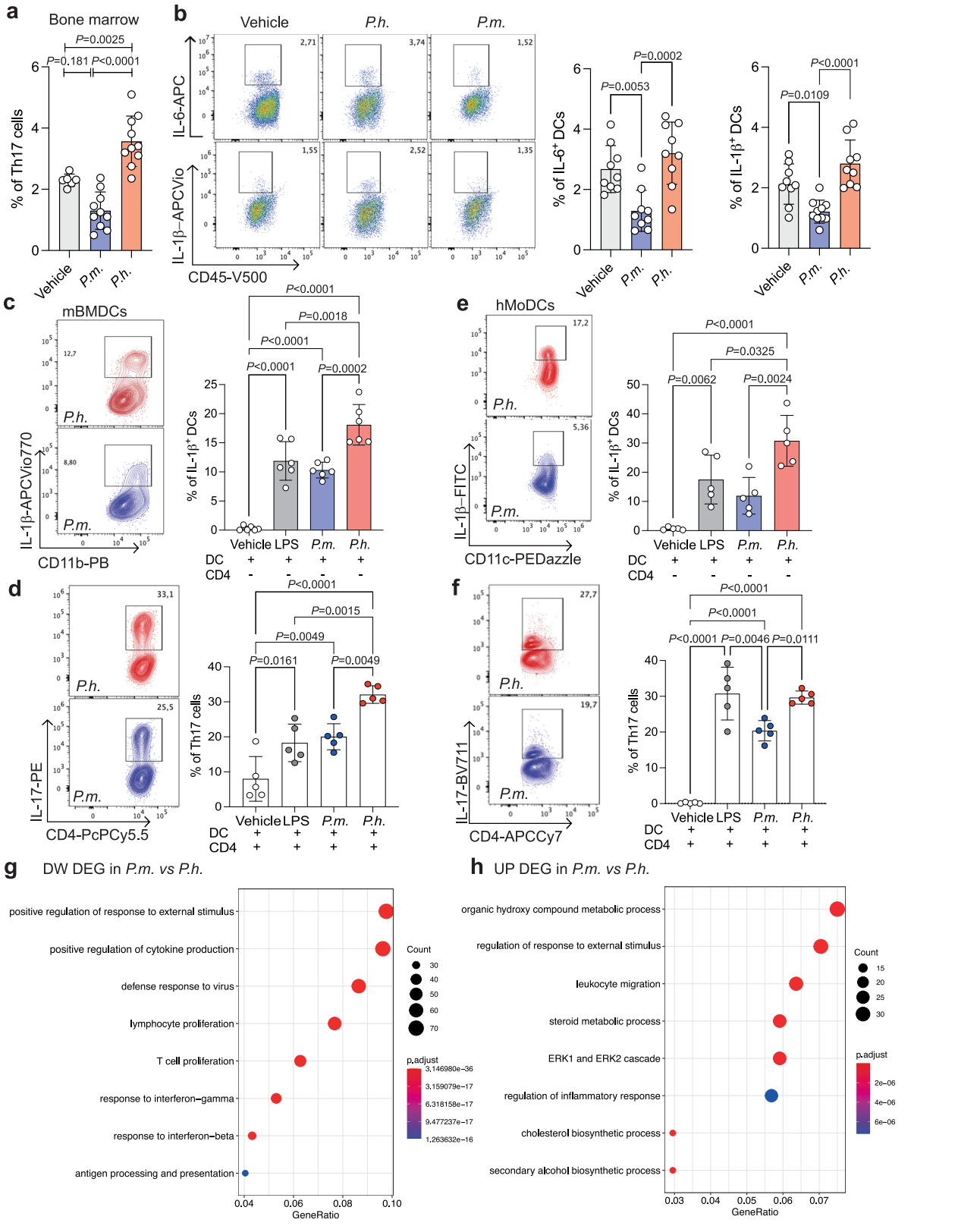

Discussion

Clinical and experimental evidence support a role for the gut microbiome in response to immunotherapies that include ICB[8,34]. Fecal microbiota transplantation (FMT) from ICB-sensitive into ICB-refractory patients induced microbiota perturbation that correlated with enhanced anti-tumor immunity and clinical benefits[35] and abrogated ICB-associated colitis[36]. Whereas several clinical trials combining FMT and ICB are underway, FMT for cancer patients is far from being standardized, it does not appear to reduce the incidence and severity of IrAEs[35], may transmit multi-drug resistant bacteria, and is therefore under scrutiny by national health agencies[37]. Administration of selected bacteria is an alternative strategy to modulate the gut microbiota[38,39]. Indeed, delivery of *P. melaninogenica* to mice affected by Early-MM delays progression to Late-MM, synergizes with anti-PD-

Fig. 4 | *P. melaninogenica* restrains proinflammatory activation of DC and limits differentiation of Th17 cells. a, **b** immunological analysis performed by flow cytometry on the BM of female t-VkMYC mice conditioned with *P.m.*, *P.h.* or unconditioned (vehicle) and euthanized at the appearance of M-spike. **a** Percentage of Th17 cells gated in $CD4^+$ T cells in the BM. Veh: $n = 6$; *P.m.* $n = 10$; *P.h.* $n = 10$ mice/group. Each dot represents one mouse. Data are presented as mean ± SD. Statistical analysis by one-way Anova. Data are pooled from two independent experiments. **b** Representative flow cytometry plots and quantification of BM $CD11c^+$ cells (DCs) producing IL-6 and IL-1β. Veh: $n = 9$; *P.m.* $n = 10$; *P.h.* $n = 9$. Each dot represents one mouse. Data are presented as mean ± SD. Statistical analysis by one-way Anova. Data are pooled from two independent experiments. Representative gating strategy is reported in Supplementary Fig. 6b. **c** Percentage of mouse BMDCs producing IL-1β upon overnight stimulation with LPS from *E.coli* (1 µg/mL), heat-inactivated *P.h.* or *P.m.* (1 mg/mL). Vehicle: Medium. Each dot represents a biological independent experiment ($n = 6$). **d** Percentage of Th17 cells (identified as $IL\text{-}17^+$ cells in $CD3^+CD4^+$ cells) obtained upon coculture of muse OT-II cells with BMDCs from (**c**). Coculture was maintained for 5 days under suboptimal Th17-polarizing conditions (see methods section). Each dot represents an independent experiment biological experiment ($n = 5$). **e** Percentage of human MoDCs producing IL-1β stimulated as in c. Each dot represents an independent experiment biological experiment ($n = 5$). **f** Percentage of Th17 cells induced upon coculture of human purified CD4 T cells with MoDCs from e. Coculture was maintained for 6 days under suboptimal Th17-polarizing conditions in the presence of Dynabeads Human T-Activator CD3/CD28. Each dot represents an independent experiment biological experiment ($n = 5$). For panels (**c**–**f**), data are presented as mean ± SD. Statistical analysis by One-way ANOVA. Representative gating strategy for panels (**b**–**f**) are reported in Supplementary Fig. 6. **g**, **h** Dot Plots of selected significantly enriched (adjusted *p*-value < 0.05) GO biological processes (BP) pathways identified from down-regulated (DW; **g**) or upregulated (UP; **h**) differentially expressed genes (DEGs). Enrichment was assessed using a one-tailed hypergeometric test, with multiple testing correction using the Benjamini-Hochberg procedure. $n = 3$ biologically independent replicates. *BMDCs* bone marrow-derived dendritic cells; *MoDCs* monocyte-derived dendritic cells. Source data are provided as a Source Data file.

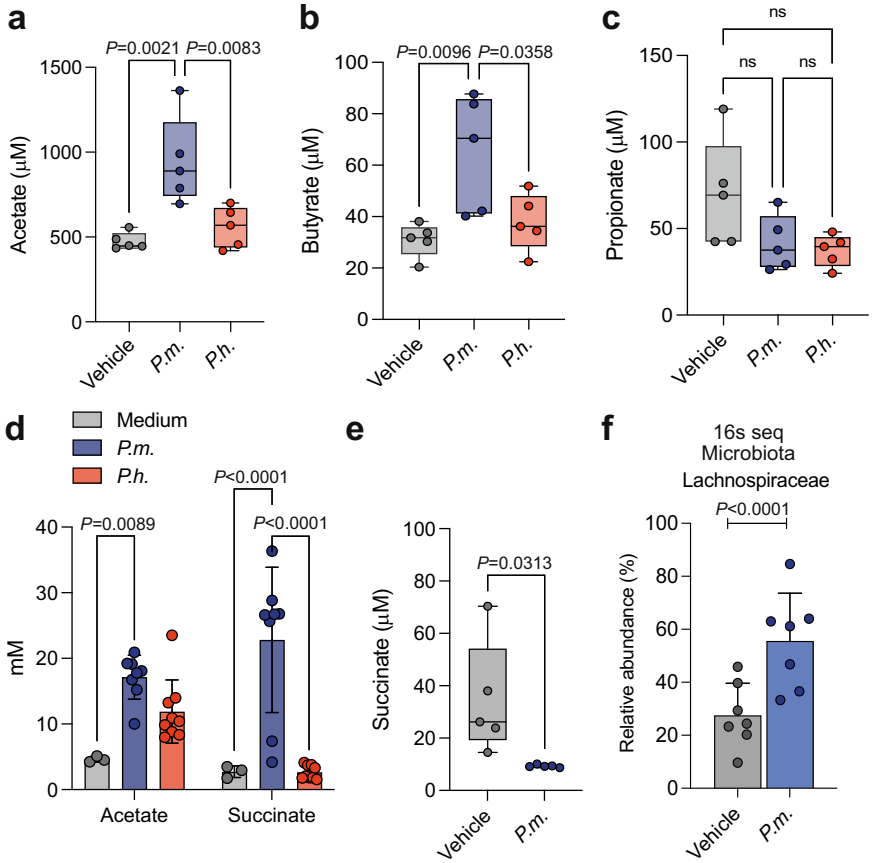

Fig. 5 | Administration of *P. melaninogenica* promotes the increase of fecal SCFAs. a–**c** NMR quantification of acetate (**a**), butyrate (**b**) and propionate (**c**) in the feces of female t-VkMYC mice treated as in Supplementary Fig. 6a. Boxplots show the distribution of values, with the central line indicating the median, box edges representing the 25th and 75th percentiles, and whiskers extending to the minimum and maximum values. Individual values represent single mice. $n = 5$ mice/group. Statistical analysis by One-way Anova. **d** Concentration of metabolites in the media metabolized by *P.m.* ($n = 8$ biological independent bacterial cultures) or *P.h.* ($n = 9$), analyzed by NMR. Medium: unmetabolized media ($n = 3$). Each dot represents a biological independent replicate. Data are presented as mean ± SD. Statistical analysis by Two-way Anova. **e** NMR quantification of succinate in the feces of t-VkMYC mice treated with *P.m.* or vehicle. Boxplots show the distribution of values, with the central line indicating the median, box edges representing the 25th and 75th percentiles, and whiskers extending to the minimum and maximum values. Each dot represents one mouse ($n = 5$ mice/group). Statistical analysis by a two-tailed unpaired *t* test. **f** Relative abundance of *Lachnospiraceae* family in the feces of *P.m.* or vehicle-treated Vk*MYC mice by 16S RNA-seq ($n = 7$ mice/group). Each dot represents one mouse. Data are presented as mean ± SD. Statistical analysis by Two-way Anova. ns: not significant. NMR: nuclear magnetic resonance. Source data are provided as a Source Data file.

L1 antibodies and contains ICB-related skin toxicity. Thus, a strategy as simple as modulating the gut microbiota may intercept MM evolution and tilt the balance in favor ICB in plasma cell dyscrasias. Our data provide a proof of concept for developing *P. melaninogenica*-based strategies for SMM patients. Further studies are needed to refine the optimal design, safety and delivery of *P. melaninogenica*-based probiotics in patients.

Administration of *P. melaninogenica* limits the expansion of Th17 cells in both the PPs patches and the BM of Vk*MYC mice, thus curbing a pathogenic mechanism. Indeed, in these mice, IL-17 may directly fuel

https://doi.org/10.1038/s41467-025-65312-y

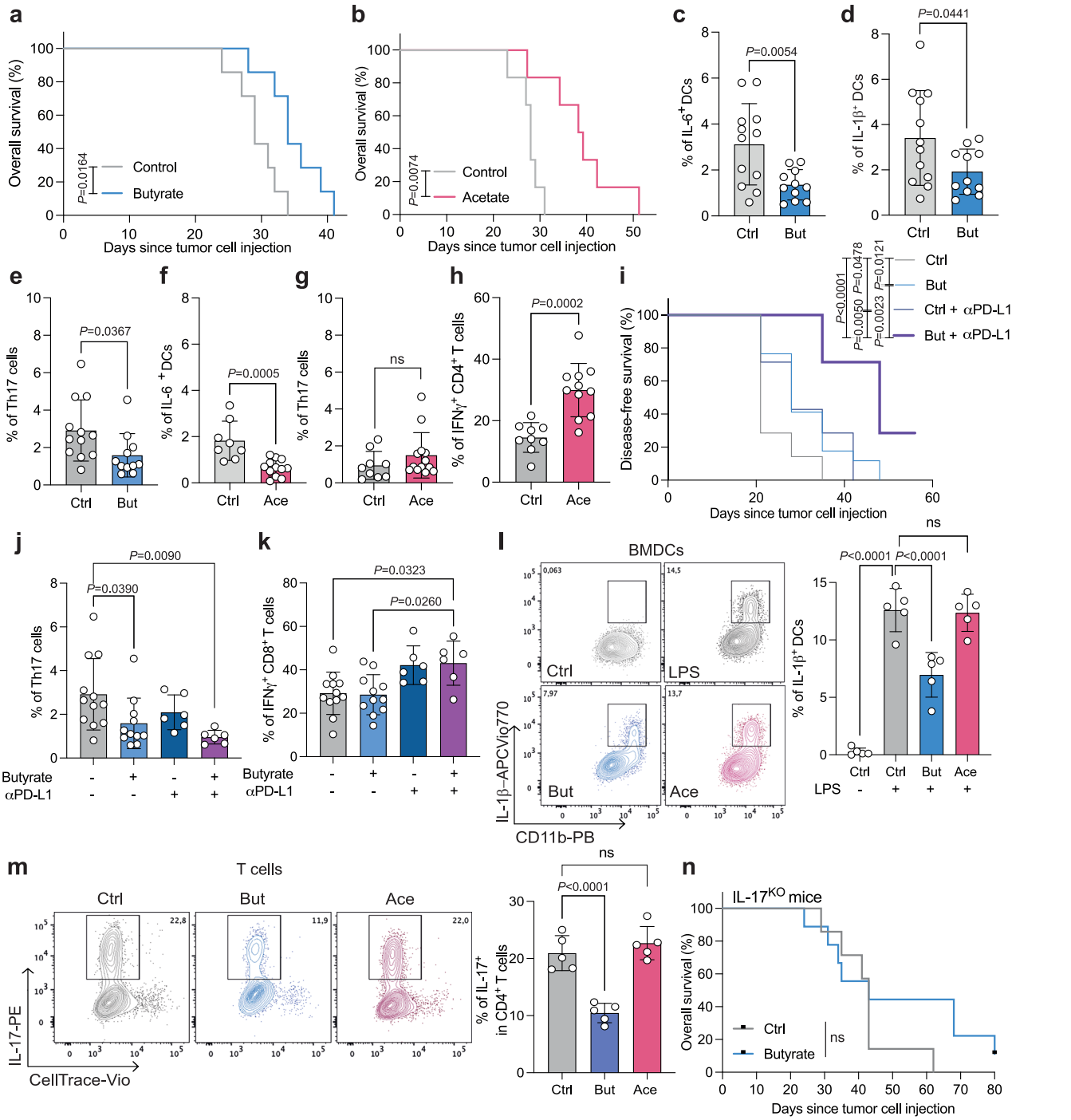

Fig. 6 | Butyrate restrains Th17 expansion and delays MM progression. a, **b** Overall survival of female t-VkMYC mice receiving sodium butyrate (But; 100 mM; $n = 7$; **a**) or sodium acetate (Ace; 200 mM; $n = 6$; **b**) dissolved in the drinking water starting two weeks before tumor injection. Control mice (**a**: $n = 7$; **b**: $n = 6$) receive plain water. Log-rank (Mantel–Cox) test. Data pooled from two independent experiments. Each dot represents one mouse. Data are presented as mean ± SD. **c**–**h**. Percentage of immune cells in the bone marrow (BM)**:** IL-6$^+$ (**c**) and IL-1β$^+$ (**d**) cells gated in CD11c$^+$. Th17 cells (**e**). IL-6$^+$ (**f**) cells in CD11c$^+$, Th17 cells (**g**) and IFNγ$^+$ cells gated in CD4$^+$ T cells (**h**). Each dot represents one mouse (c-e: Ctrl $n = 12$; But $n = 11$; (**f**–**h**): Ctrl $n = 9$; Ace $n = 13$). Data are presented as mean ± SD. Two-tailed unpaired *t* test. Gating strategy to detect CD11c + cells in the BM is shown in Supplementary Fig. 6b. **i** M-spike appearance since tumor injection of t-VkMYC mice fed butyrate or control and treated with αPD-L1 (200μg, three times/week) starting one week after tumor injection. Ctrl $n = 14$; Butyrate $n = 17$; Ctrl + αPD-L1 $n = 7$; Butyrate + αPD-L1 $n = 7$. Data pooled from three independent experiments. Statistical analysis by Log-rank (Mantel–Cox) test. **j**, **k** Percentage of Th17 cells (**j**) and IFNγ$^+$CD8$^+$ cells (**k**) in the BM. Each dot represents one mouse. Ctrl $n = 12$, But $n = 11$, Ctrl + αPD-L1 $n = 6$, But + αPD-L1 $n = 6$. Data are presented as mean ± SD. One-way Anova. **l** Representative plots and percentage of IL-1β$^+$ BM-derived DCs differentiated in the presence of butyrate or acetate (1 mM)-conditioned media. Each dot represents a biologically independent experiment performed in triplicate ($n = 5$). Data are presented as mean ± SD. Statistical analysis by One-way Anova. **m** Representative plots and percentage of Th17 cells after 5 days of culture under Th17-polarizing conditions in butyrate or acetate (0.5 mM)-conditioned media. Each dot represents a biological independent experiment performed in triplicate ($n = 5$). Data are presented as mean ± SD. Statistical analysis by One-way Anova. **n** Overall survival of IL-17KO t-VkMYC mice fed butyrate ($n = 9$) or control ($n = 7$). Both male and female mice were included in experimental groups as reported in Supplementary Fig. 9. Data pooled from two experiments. Log-rank (Mantel–Cox) test. ns: not significant. Source data are provided as a Source Data file.

https://doi.org/10.1038/s41467-025-65312-y

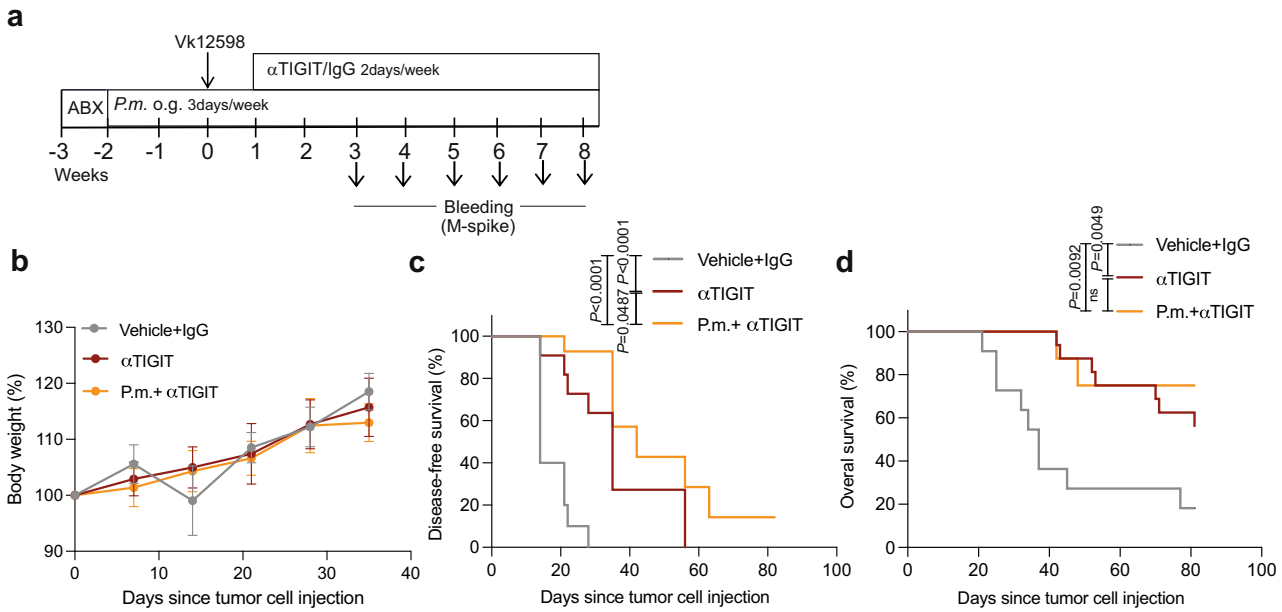

Fig. 7 | *P. melaninogenica* combined with anti-TIGIT antibodies delays MM onset. a Treatment schedule for female C57BL/6 mice injected with Vk12598 MM cells (t-VkMYC) conditioned with *P.m.* or vehicle (PBS) and receiving αTIGIT or IgG. **b** Body weight variation since tumor cell injection. Vehicle + IgG: $n = 10$; Veh + αTIGIT: $n = 11$; *P.m.*+ αTIGIT: $n = 14$. Data are presented as mean ± SD. Statistical analysis by One-way Anova. **c**, **d** M-spike appearance since tumor injection (**c**) and overall survival (OS; **d**). Vehicle + IgG: $n = 10$; Veh + αTIGIT: $n = 11$; *P.m.*+ αTIGIT: $n = 14$. Data pooled from two independent experiments. Statistical analysis by Log-rank (Mantel–Cox) test. ns: not significant. Source data are provided as a Source Data file.

plasma cell survival and promote disease progression[6]. DCs are strongly affected by *Prevotellae* because ex vivo, less DCs from the BM of *P. melaninogenica*-treated mice produce IL-6 and IL-1β when compared to mice challenged with *P. heparinolytica*. These findings were confirmed in vitro by RNASeq and functional assays on DCs stimulated with *P. melaninogenica*. Conversely, *P. heparinolytica*-conditioned DCs show a more proinflammatory transcriptomic profile and generate more Th17 than *P. melaninogenica*-treated DCs. These findings highlight the distinct immunomodulatory effects of the two *Prevotella* species. Because hMoDCs similarly respond in vitro to the two *Prevotellae*, administering *P. melaninogenica* to patients affected by plasma cell dyscrasias should be beneficial.

Our data also support the in vivo beneficial effects of SCFAs. Indeed, more SCFAs are found in the stools of *Prevotella*-treated mice, and *P. melaninogenica* associates with much higher stool content of acetate and butyrate. Because in vitro *P. melaninogenica* generates acetic and succinic acids[40], which is consistent with our in vivo findings, we argue that *P. melaninogenica* also modulates the gut microbiota in favor of butyrate-producing bacteria, which transformed succinate in butyrate[27]. Similarly, enrichment of butyrate-producing bacteria at the expenses of MM-associated dysbiosis, provide survival advantage in MM-bearing mice[41,42].

Butyrate and acetate boost the effector function of cytotoxic T lymphocytes[30,32] and their memory potential[30]. Butyrate also interferes with DC maturation and cytokine secretion[43]. Here, we confirm the antitumor potential of both molecules in t-VkMYC mice, supporting their positive association with MM outcomes. Our data showing that butyrate delays disease appearance by acting on DCs and directly restraining Th17 cells provides additional information on the in vivo beneficial effects of butyrate in MM patients[25,44,45]. SCFAs may also be beneficial in limiting BM damage, a clinical culprit of MM[46] because Th17 cells contributes to bone destruction[47], and restraining Th17 expansion in MM patients by administering *P. melaninogenica* might impact bone formation. On the same line, butyrate stimulates bone formation through the secretion of Wnt10b by BM $CD8^+$ T cells[48]. Likely, the beneficial activity of *P. melaninogenica* extends beyond SCFA production.

While we did not measure the content of SCFAs in the stools of Vk*MYC mice treated with *P. melaninogenica* or vehicle as we did in t-VkMYC mice, we believe our data support an analogous mechanism of action for *P. melaninogenica* in the two experimental settings. Our conclusion is based on the evidence that both Vk*MYC and t-VkMYC mice experience less aggressive disease upon treatment with *P. melaninogenica*. In both models, treatment with *P. melaninogenica* associates with less BM Th17 cells. The gut microbiota in Vk*MYC treated with *P. melaninogenica* is enriched in butyrate-generating bacteria, and more butyrate is found in stools from t-Vk*MYC mice treated with *P. melaninogenica*. Finally, DCs cultured in vitro in the presence of either *P. melaninogenica* or butyrate mimic the functional characteristics of DCs obtained from the BM of mice either treated with *P. melaninogenica* or butyrate.

An additional novelty of this paper is that combining *P. melaninogenica* and anti-PD-L1 antibodies uncouples efficacy and toxicity of ICB in a model of MM. PD-L1 was chosen as a representative ICB because PD-L1 is expressed on neoplastic plasma cells, anti-PD1/PD-L1-based immunotherapy has been already tested in patients affected by MM, and caused severe IrAEs[11]. In addition, gut microbiota composition has been associated with improved response to immunotherapy[8], and defined microbiota signatures have been associated with IrAEs[13,14], which can be induced by IL-17-producing cells[15]. Our findings strongly support the use of gut microbiota-modulating strategies to manage IrAEs and warrant further investigation on *P. melaninogenica* as a potential candidate for such treatment. Our data also show the potential beneficial effects of combining *P. melaninogenica* and TIGIT, a target with promising translational potential in a clinical setting[33].

Mechanistically, *P. melaninogenica* limits the expansion of Th17 cells, thus inhibiting a pro-tumorigenic mechanism in MM[7]. Conversely, *P. melaninogenica* does not restrain the cytotoxic response elicited by ICB, providing treated animals with a more favorable $CD8^+$ $IFN\gamma^+$/Th17 ratio. Interestingly, IL-17 was found elevated in microsatellite-stable CRC, and blocking IL-17 enhanced the efficacy of anti-PD-1 therapy in mouse models of CRC[49]. IL-17 also supports the clinical benefit of dual CTLA-4 and PD-1 inhibition in melanoma

patients[50]. These data appear at odd with those reporting that low baseline butyrate was associated with longer PFS in patients affected by metastatic melanoma[51]. Thus, *P. melaninogenica* and SCFA-producing commensals might not be indicated when IL-17 is anti-tumoral. Conversely, *P. melaninogenica* and ICB might synergize in patients affected by other hematologic and solid tumors in which IL-17 acts as a driving force[7].

We have also found that modulation of the gut microbiome with SCFA-producing bacteria limits IrAEs. This effect again appears related to the ability of *P. melaninogenica* to limit Th17 cell expansion, especially in skin-draining lymph nodes. Interestingly, mIHC analyses of the skin from mice receiving imiquimod, anti-PD-L1 antibodies, and *P. melaninogenica* shows reduced density of gut-homing (i.e., $\alpha4\beta7^+$) cells, supporting restrained migration of cells from the gut into the skin of mice receiving *P. melaninogenica*. $CD11c^+$ cells are also less represented and tended to be more distant from CD4 T cells in *P. melaninogenica*-treated mice, suggesting that the intestinal commensal in this model of skin toxicity also impacted APCs.

IL-17 is involved in several IrAEs[52], ICB may unleash commensal-specific Th17 responses leading to skin toxicity[14], and IL-17 blockade reversed psoriatic rash in one patient treated with pembrolizumab[53]. Inhibition of IL-17 also abrogated nivolumab-associated colitis and protected mice against ICB-induced thyroiditis[54]. ICB-induced colitis can be ameliorated by treating mice with *Bifidobacterium*, which favors the expansion of Tregs[55], a mechanism distinct form *P. melaninogenica*. Thus, *P. melaninogenica*, by producing SCFAs and restraining Th17 cell expansion, might positively impact additional IrAEs.

The finding that *P. melaninogenica* administration protects mice with plasma cell dyscrasias from aggressive disease might suggest that SMM patients harboring this commensal are naturally protected from multiple myeloma (MM) progression. To our knowledge, no publicly available databases provide information on the relative abundance of *P. melaninogenica* in fecal samples from SMM patients who either progressed or did not progress to MM. A Spanish group[25] reported enrichment of *Prevotella* at the genus level in healthy controls compared to newly diagnosed MM patients. There also was a trend in progressive reduction of *P. melaninogenica* relative abundance from healthy controls to MGUS to SMM patients. Interestingly, acetate levels were significantly lower in the blood serum of SMM patients compared to the MGUS group[25]. Jian and colleagues[41] found enriched *Prevotella* strains, including *P. ruminicola*, *P. fusca*, and *P. melaninogenica*, in newly diagnosed Chinese MM patients compared to healthy controls. Different *Prevotella* strains may exert opposing effects[7], and like *P. copri*[56], different strains of *P.melaninogenica* might exist, exerting varying and even opposing effects on human health[57]. *P. melaninogenica* clades might differ among human populations globally, and, as we documented in mice gavaged with *P. melaninogenica*, these differences could variously impact the entire gut microbiome. While these considerations should not diminish the potential value of *P. melaninogenica* for human health, clinical studies are warranted to define its beneficial activity in patients with plasma cell dyscrasias.

Microbiota perturbation holds safety issues. Abundance of *P. melaninogenica* together with other commensals were found in the lung of patients affected by cystic fibrosis[58], in the oral cavity of children with active caries[59] and in the gut of patients affected by ankylosing spondylitis[60]. These data suggest that in selected clinical conditions, clades of *P. melaninogenica* may act as pathobionts. While daily administration of *P. melaninogenica* to mice promoted gastric inflammation[61], intranasal administration of *P. melaninogenica* did not cause any damage to healthy mice, but it enhanced bleomycin-induced lung immune infiltration and fibrosis[62]. Conversely, *P. melaninogenica* suppressed experimental autoimmune encephalomyelitis in HLA-DR3.DQ8 transgenic mice[63]. Different outcomes may relate to different experimental settings and/or strains of *P. melaninogenica,* as reported for *P. copri*[56]. We also cannot exclude that *P. melaninogenica* drove dissimilar reconstitution of the microbiota community in the various experimental settings described above.

One limitation of the study is that antibiotic pretreatment is needed to fully unleash the beneficial effects of *P. melaninogenica*. Antibiotics cause dysbiosis, and their use may associate with worst prognosis in MM[44]. Previous research in mice showed that using antibiotics to aid probiotic colonization[41,64] didn't prevent the same bacterial strains from being used in humans without antibiotics[65,66]. While we cannot anticipate that antibiotic pretreatment might be needed in humans, the promising results obtained in Vk*MYC mice treated with *P. melaninogenica* should outweigh the potential disadvantage of one cycle of antibiotics in patients affected by SMM.

Altogether, our results support *P. melaninogenica* or SCFAs administration as a strategy that might be sufficient per se to modify the trajectory of patients affected by SMM. The combination of *P. melaninogenica* and ICB might also represent an additional strategy to uncouple efficacy and toxicity of ICB and limit MM aggressiveness.

Methods

Mice

All mice were on a C57BL/6 background. IL-17KO mice[67] were kindly provided by Dr. Yoichiro Iwakura (Institute of Medical Science, Tokyo, Japan). Experimental procedures with IL-17KO mice were initiated when animals were between 6 and 8 weeks of age. Six-eight-week-old C57BL/6 J female mice were purchased from Charles River Laboratories, Calco IT (stock number 000664). In Vk*MYC transgenic mice[4] the activation of MYC, whose locus is rearranged in half human MM tumors, including SMM[68], occurs sporadically through the somatic hypermutation process in germinal center B cells. All Vk*MYC mice were born from 12/2020 to 11/2021 and included in the experiment from 09/2021 to 06/2022 (mean age at inclusion: 37 ± 5 weeks; median age at inclusion 40 weeks). All mice were randomly assigned to each treatment and monitored for disease progression for up to 26 weeks. Data from each Vk*MYC mouse present in this study are available in the Supplementary data 1. Both male and female mice were used in Vk*MYC and IL-17KO models, with no significant differences observed between sexes. Primers sequences for the genotype of Vk*MYC and IL-17KO mice are reported in Supplementary Table 3. Vk*MYC and IL-17 knockout (IL-17KO) mice were bred and maintained under specific pathogen-free (SPF) conditions. For experiments involving Vk12598 cell injections, mice were housed in a non-barrier animal facility. In studies involving microbiota manipulation, experimental and control groups were housed separately following randomization to prevent cross-contamination. Mice were housed under 12h light/12h dark cycle, at temperatures of 23 ± 2 degree Celsius and 50% ± 10 humidity. Mice were euthanized using carbon dioxide (CO_2) inhalation followed by confirmation of death in accordance with institutional animal care guidelines. Animal procedures were approved by the institutional animal ethics committee (Italian Ministry of Health authorization No. 208/2023-PR and n. 259/2025-PR).

Injection of Vk12598 cells and generation of t-VkMYC model

Vk12598 cells were obtained by transplantation of Vk*MYC tumor cells from a male Vk*MYC donor into congenic mice as described by Chesi et al.[18]. Transplanted cells were propagated by serial transplantation into congenic wild-type mice. Briefly, 10^6 cells were injected in the tail vein of C57BL/6 mice. Disease appearance and progression was monitored by quantification of monoclonal immunoglobulins by serum protein electrophoresis. The spleen of transplanted animals was collected at sacrifice, cells were harvested under sterile conditions and stored in liquid nitrogen for subsequent transplantation.

Bacteria cultivation

P. melaninogenica DSM 7089 and *P. heparinolytica* DSM 23917 (DSMZ, Germany) were cultured in chocolate agar plates at 37 °C in AnaeroJar

2.5 L Jar System (OXOID: Cat. AG0025A; ThermoFisher Scientific) and using AnaeroGen 2.5 L (Cat. AN0025A, ThermoFisher Scientific) to generate an anaerobic atmosphere. *Staphylococcus epidermidis*, isolated from a biological sample, was cultured on chocolate agar plates at 37 °C under aerobic conditions.

Bacteria and antibody treatment in vivo

SMM Vk*MYC mice[5] were pretreated for one week with Ampicillin (1 g/L, Cat. A9393, Sigma-Aldrich), Vancomycin (0.5 g/L, Cat. 94747, Sigma-Aldrich) and Neomycin (1 g/L, Cat. N1876, Sigma-Aldrich) dissolved in drinking water and Metronidazole (0.2 mg/mouse, Cat. M3761, Sigma-Aldrich) via gavage three times. 48 h after antibiotic withdrawal, *P. melaninogenica* was administered via gavage for three consecutive days/week until the end of the experiment. 1.5×10^8 colony-forming units (CFUs) were provided with each gavage. Control mice received gavage with saline solution (PBS). A preliminary experiment in t-VkMYC mice demonstrated that antibiotic pretreatment was required to enable the biological activity of *P. melaninogenica* (Supplementary Fig. 1i, j). Anti-PD-L1 (B7-H1, clone 10 F.9G2, Cat. BE0101, BioxCell; 200 μg/dose) or isotype antibodies (Rat IgG2b, Cat. BE0090, BioxCell) were injected i.p. on day 0, 5, 8, and every three weeks until the end of the experiment. Every three weeks, mice were bled for monoclonal (M) protein (M-spike) quantification as described in below. Mice were euthanized when progressing to Late-MM or at the end of observation time. Late-MM progression was defined by M-spike was ≥6% (i.e., gamma/albumin ratio ranging between 0.35 and 0.75) and the presence of anemia. Alternatively, two weeks before tumor cell injection (i.v. 1×10^6 Vk12598 cells obtained from one MM Vk*MYC mouse; t-VkMYC[4]), antibiotic-pretreated WT mice were subjected to gavage either with *P. melaninogenica*, *P. heparinolytica*, *Staphylococcus epidermidis*, or PBS (according to the experiment) and received anti-PD-L1/IgG three times/week. Anti-TIGIT antibodies (Clone 1G9, Cat. BE0274, BioxCell) or isotype control antibodies (mouse IgG1 isotype; Cat. BE0083, BioxCell; 200 μg/dose) were administered twice per week to t-VkMYC mice pretreated as described above. t-VkMYC mice were weekly bled for M-spike quantification. For immunological experiments, mice were euthanized by CO_2 inhalation at M-spike appearance between week 3 and 6 after tumor cell injection, and harvested organs were analyzed as described below. The list of antibodies used for flow cytometry analysis is reported in supplementary Table 2.

Butyrate and acetate treatment

Sodium butyrate (working concentration of 100 mM; Cat. 303410, Sigma-Aldrich) or sodium acetate (working concentration of 200 mM; Cat. S5636, Sigma-Aldrich) were dissolved in drinking water starting two weeks before tumor injection (t-Vk*MYC mice). Solution was refreshed b.i.w. Control mice received plain water.

Imiquimod-induced skin inflammation

Antibiotic-pretreated mice received oral gavage of *P. melaninogenica, P. heparinolytica* or PBS until the end of the experiment. Three doses of anti-PD-L1 or IgG antibodies (of 200 μg each) were injected i.p. every 4 days. Subsequentially, mice received a topical dose of 62,5 mg of Imiquimod cream (5%) (Aldara; 3 M Pharmaceuticals) on the shaved skin of the back for 7 consecutive days. Each dose corresponded to 3125 mg of active compound. On day 7, mice were euthanized, and organs were collected. Briefly, the back cutaneous tissue was collected and fixed in formalin solution for 24 h before inclusion for histopathological evaluation. Inguinal lymph nodes were collected and gently disaggregated with the help of tweezer and single-cell suspension processed for flow cytometry staining. For the experiment in the t-VkMYC model, antibiotic-pretreated mice received oral gavage of *P. melaninogenica, P. heparinolytica* or PBS until the end of the experiment. Two weeks after the first gavage, mice were injected with Vk12598 tumor cells and anti-PD-L1 or IgG antibodies (of 200 μg each) were injected i.p. every 4 days. Four weeks after tumor injection, mice received imiquimod cream for 7 consecutive days as described above and subsequently euthanized for organ collection.

Serum protein electrophoresis

Mouse blood was periodically collected. Semi-automated electrophoresis was performed on the Hydrasys instrument (Sebia, Lissex, France). According to the manufacturer's instructions, 10 μL of undiluted serum were manually applied to the Hydragel agarose gels (Sebia). The subsequent steps: electrophoresis (pH 9.2, 20 W constant current at 20 °C), drying, amidoblack staining, de-staining and final drying were carried out automatically. The use of Hydrasys densitometer and Phoresis software (Sebia) for scanning resulting profiles provided accurate relative concentrations (percentage) of individual protein zones. M-spike levels were calculated as total gamma globulins/albumin ratio (γ/albumin).

Multiplex immunohistochemistry (mIHC)

The Tyramide Signal Amplification (TSA)-based Opal method (Akoya Biosciences, Marlborough, MA, USA) was used for mIHC staining on the Leica BOND RX automated immunostainer (Leica Biosystems, Wetzlar, Germania). All stains were performed under optimized conditions. The spectral DAPI (Akoya) was used as a nuclear counterstain, and slides were mounted in ProLong Diamond Anti-fade Mountant (Life Technologies, Waltham, MA, USA). An unstained tissue section was used to subtract the tissue autofluorescence from multiplex-stained slides. Primary antibodies are listed in Table S2.

mIHC imaging and analysis

Multiplex stained slides were imaged using the Mantra Quantitative Pathology Workstation (Akoya Biosciences, Marlborough, MA, USA) at 20X magnification. The inForm Image Analysis software (version 2.4.9, Akoya Biosciences, Marlborough, MA, USA) was used to unmix multispectral images. A selection of representative multispectral images was used to train the inForm software to create algorithms to apply in the batch analysis of all acquired multispectral images. phenoptrReports (add-ins for R Studio from Akoya Biosciences) was used to calculate cell density and spatial metrics. Cell density data were calculated as the sum of the cells positive for a specific marker, divided by the area analyzed from the same tissue slide. For the mean distance between different cell subtypes, the nearest neighbor analysis was used.

Histopathological evaluation and scoring severity of skin inflammation

Histopathological evaluation was performed in blind by two expert pathologists on 2 H&E-stained slides of the skin for mouse. Hyperkeratosis, acanthosis, spongiosis, and inflammatory infiltrate were scored independently on a scale from 0 to 4: 0, none; 1, slight; 2, moderate; 3, marked; 4, very marked.

In vitro induction of mouse BM-derived dendritic cells

BM cells collected from long bone flushing were cultured for 6 days in IMDM (Lonza Bioscience) with 10% FCS (Fetal Calf Serum), GM-CSF (25 ng/mL; Cat. 315-03, PeproTech, Inc.) and IL-4 (5 ng/mL; PeproTech). DCs were induced to overnight maturation with 1 mg/mL heat-inactivated *P.heparinolytica*, *P. melaninogenica* or 1 μg/mL LPS from *E.coli*. To evaluate DC activation in the presence of SCFAs, butyrate or acetate (1 mM; Sigma-Aldrich) were dissolved into the culture medium three days after seeding and maintained until the end of the culture.

In vitro induction of human monocyte-derived DCs

$CD14^+$ monocytes were isolated by magnetic sorting (Cat. 130-050-201, Miltenyi Biotec) from healthy donor's peripheral blood mononuclear cells (PBMCs) and cultured in RPMI (Lonza Bioscience) with 10% FCS,

GM-CSF (50 ng/ml; Cat. 300-03, Peprotech, Inc) and IL-4 (25 ng/ml; Cat. 200-04, Peprotech, Inc). DC maturation was induced as described above.

Mouse Th17 induction with bacteria-stimulated DCs

Splenocytes from OTII mice[22] were pulsed with 50 μg/10^6 cells of $OVA_{323–339}$ peptide for 1 h and then plated at 10:1 ratio with mature BMDCs. Coculture was maintained for 5 days with half of the optimal cytokine concentration for the induction of Th17 cells and in the absence of IL-1β: TGF-β (2 ng/mL; Cat. 100-21 C, Peprotech, Inc.), IL-6 (10 ng/mL; Cat. 216-16, Peprotech, Inc.). anti-mouse IFNγ (10 μg/mL; Cat. 505834, Biolegend, Inc) and anti-mouse IL-4 (10 μg/mL; Cat. 504122, Biolegend, Inc) were added to the culture to inhibit differentiation towards Th1 and Th2, respectively.

Human Th17 induction with bacteria stimulated DCs

Starting from healthy donor's PBMC $CD14^-$ fraction, CD4 + T cells were isolated by magnetic sorting (Cat. 130-094-131, Miltenyi Biotec) and plated at 10:1 ratio with HLA-matched MoDCs preconditioned with bacteria as described above. Dynabeads™ Human T-Activator CD3/CD28 (Cat. 11161D, ThermoFisher Scientific) were added to the culture. Coculture was maintained for 6 days in the presence of half of the optimal cytokine concentration for the induction of Th17 cells: IL-6 (1,12 ng/mL, Cat. 200-26, Peprotech, Inc.), IL-23 (15 ng/mL; Cat. 200-23, Peprotech, Inc). Anti-human IFNγ (1 μg/mL; Cat. 506532, Biolegend, Inc) and anti-human IL-4 (2 μg/ml; Cat. 500838, Biolegend, Inc) were added to the culture to inhibit differentiation towards Th1 and Th2, respectively.

Conditioning of mouse Th17 cells with SCFAs

Mouse-derived splenocytes were stained with CellTrace™ Violet Cell Proliferation kit (Thermo Fisher) and cultured in vitro for 5 days with Dynabeads™ Mouse T-Activator CD3/CD28 (Cat. 11452D, ThermoFisher Scientific) under optimal Th17-polarizing conditions: TGF-β (2 ng/mL; Cat. 100-21 C, Peprotech, Inc.), IL-6 (20 ng/mL; Cat. 216-16, Peprotech, Inc.), IL-1β (10 ng/mL; Cat. 130-101-680, Miltenyi Biotech). anti-mouse IFNγ (10 μg/mL; Cat. 505834, Biolegend, Inc) and anti-mouse IL-4 (10 μg/mL; Cat. 504122, Biolegend, Inc) were added to the culture to inhibit differentiation towards Th1 and Th2, respectively. At day 0 sodium acetate or sodium butyrate (Sigma-Aldrich) were added to the medium at 1 mM working concentration and maintained for the entire experiment.

Bulk RNASeq

mRNA was extracted with the RNeasy Mini Kit (Qiagen) from 10^6 mouse BMDCs after an overnight stimulation with heat-inactivated bacteria as described above. Prior to library preparation, the quality of RNA samples was assessed using the TapeStation 4100 (Agilent) to determine the RNA Integrity Number (RIN) for each sample. NGS libraries were then constructed utilizing the TruSeq Stranded mRNA (Illumina) protocol, which permits library preparation starting from 5–100 ng of total RNA. These libraries were subsequently barcoded, pooled, and sequenced on a NovaSeq 6000 (Illumina, San Diego, CA) sequencing system. Each RNA library yielded approximately 20–30 million reads, configured in single-read mode with a length of 100 nucleotides. Raw data underwent demultiplexing using the latest version of Bcl2Fastq (Illumina). Sequencing was performed on an Illumina NovaSeq6000 system (single-end, 100 bp read length). Reads were trimmed with Trimmomatic (v0.39) to remove adapters and exclude low-quality reads from the analysis, and aligned to the mouse GRCm38 reference genome using the STAR aligner (v2.5.3a). FeatureCounts (v1.6.4) was used to compute reads mapping on exons as annotated in GENCODE mouse basic gene annotation M22 and obtain transcript quantification summarized at the gene level, excluding multimapping reads. Only genes with at least 1 CPM (Counts per million) in at least 3 samples were retained. Differential gene expression analysis was performed with DESeq2[69] bioconductor library (v1.30.1). Dot Plots of significant pathways were generated with the ClusterProfiler R package on differentially expressed genes (DEGs)[70]. GSEA enrichments were performed with clusterProfiler (4.3.0) using GSEA C2, C5, and C7 genesets and graphically represented with enrichplot (1.10.2).

NMR-based metabolomic analysis

For fecal short-chain fatty acid quantification, feces were resuspended in buffer (PBS pH 7.4,10% D_2O and 0.01% NaN_3; ratio 1:10 mg feces:μL buffer). Samples were centrifuged for 5′ at 10.000 rpm and supernatants were collected. 50 μM of 3-(Trimethylsilyl)propane-1-sulfonic (TSP) acid was added to samples. For metabolomic of the fermented media, 20 μL of TSP 10 mM in deuterated-PB 10 mM, pH 7.4 and 0.01% NaN_3 were added to 180 μL of each sample. TSP was used as a reference for concentrations and chemical shift. All spectra were acquired at 25 °C on a Bruker Avance III 600 MHz spectrometer. ^{1}H NMR spectra were recorded with *noesygppr1d*, *cpmgpr1d* and *ledbpgppr2s1d* pulse sequences in Bruker library and 256 scans, spectral width 20 ppm, relaxation delay 6 s. They were processed with 0.3 Hz line broadening, automatically phased and baseline corrected. Chemical shifts were internally calibrated to the TSP peak at 0.00 ppm. ^{1}H,^{1}H TOCSY (Total Correlation SpectroscopY) spectra were acquired with 48 scans and 512 increments, 80 ms mixing time and relaxation delay 1.5 s. ^{1}H,^{13}C HSQC (Heteronuclear Single Quantum Coherence) spectra were acquired with 64 scans and 512 increments, relaxation delay 1.5 s. MestReNova software package (MestReNova v 14.3.0-30573, Mestrelab Research, Santiago de Compostela, Spain) was used for spectra processing and peak picking. Resonance assignment and compound identification were done with the support of 2D NMR spectra, in-house libraries and the online databases *Human Metabolome Database* (HMDB, http://www.hmdb.ca), *Biological Magnetic Resonance Data Bank* (BMRB, http://www.bmrb.wisc.edu) and *Birmingham Metabolite Library* (http://www.bml-nmr.org). The MNova GSD (Global Spectrum Deconvolution) algorithm was employed to deconvolute the overlapping regions, allowing the absolute quantification for metabolites with resonances in crowded spectral areas. The Simple Mixture Analysis (SMA) tool (https://mestrelab.com/software/mnova/sma/) integrated in MestreNova allowed to set a semi-automatic protocol for metabolite identification and quantification.

Isolation of single cell suspension and flow cytometry

At Early-to-Late-MM progression (VK*MYC) or at M-spike appearance (t-VlMYC), animals were euthanized and tissues collected. Mouse bones were harvested, and epiphyses were cut to collect BM cells. Peyer's Patches were removed from the Small Intestine of the same animals and gently disaggregated with the help of tweezers. Mesenteric or inguinal lymph nodes were collected and gently disaggregated with the help of tweezers in medium RPMI supplemented with 10% fetal calf serum (FCS). Spleen was collected and mechanically dissociated to obtain single-cell suspension. Single cell suspensions were labeled with fluorochrome-conjugated monoclonal antibodies (Supplementary Table S1) and acquired by BD FACSCanto™ II, BD FACSymphony™ A5 (BD Bioscience) or CytoFLEX LX (Beckman Colter). Cells were also assessed for intracellular cytokine production after stimulation with Phorbol Myristate Acetate (PMA) (1 mg/mL; Cat. HY-18739, MedChemExpress) and ionomycin (1 mg/mL; Cat. HY-13434, MedChemExpress) in the presence of Brefeldin A (BFA; 10 μg/mL, Cat. HY-16592, MedChemExpress). After incubation, cells were washed and stained for surface markers, fixed and permeabilized with Fixation/Permeabilization Kit (Cat. 00-5523-00, ThermoFisher Scientific) or with paraformaldehyde 2% and saponin. Cells were then washed and stained for intracellular markers. Data were analyzed using the FlowJo software (Treestar Inc). Doublets were excluded using FSC-A/FSC-H, and dead cells excluded using a viability dye. For mouse-derived

tissues, immune cells were selected for CD45 staining-positivity. All subsequent gating that differs is included within each figure. The absolute number of each cell population was normalized to the total count of live cells in the entire organ. For Peyer's patches, the number of live cells was determined from a total of five patches collected per mouse.

Sequencing of fecal microbiota

Total DNA was extracted from fecal samples of treated mice using the QIAamp PowerFecal Pro DNA Kit (Qiagen, cat. 51804), following the manufacturer's instructions. The V3-V4 region of the 16S rRNA gene was amplified from 500 ng of extracted DNA using AccuPrime Taq DNA Polymerase (Invitrogen, cat. 12346086) and the following primers: V3-16S-Fw: TCG TCG GCA GCG TCA GAT GTG TAT AAG AGA CAG CCT ACG GGN GGC WGC AG and V4-16S-Rev: GTC TCG TGG GCT CGG AGA TGT GTA TAA GAG AGA CAG GAC TAC HVG GGT ATC TAA TCC. The amplification protocol consisted of an initial denaturation at 94 °C for 2min, followed by 35 cycles of 94 °C for 30s, 56 °C for 30s, and 68 °C for 1min, with a final hold at 4 °C. Amplicons were purified using AMPure XP beads (Beckman Colter, Brea, USA). A second PCR step was performed to index the samples and add Illumina sequencing adapters. The Nextera XT Index Kit (Illumina) and the KAPA HiFi HotStart PCR Kit (KAPA Biosystems) were used with the following amplification protocol: 95 °C for 3min, followed by 8 cycles of 95 °C for 30s, 55 °C for 30s, and 72 °C for 30s, with a final extension at 72 °C for 4min, then stored at 4 °C. A second purification step with AMPure XP beads was performed to prepare the final library. Purified DNA was quantified using the Qubit dsDNA HS Assay Kit on a Qubit 2.0 Fluorometer (Life Technologies), then diluted and pooled following the Illumina protocol. Sequencing was performed on the Illumina MiSeq platform using a 600-cycle (2 × 300 bp) paired-end read protocol. Sequences with high quality scores and length > 250 bp were selected for taxonomic analysis using QIIME2 (Quantitative Insights Into Microbial Ecology v2022.2). β-diversity was calculated and generated by using principal coordinates analyses (PCA), with the derivation of weighted UniFrac and unweighted UniFrac distance matrices. PERMANOVA and Kruskal-Wallis analyses were used for assessing the statistical significance of β and α-diversity, respectively.

Statistical analysis

Sample size was chosen considering the means of target values between experimental and control groups, standard deviation and statistical analyses used. Animals were matched for age and sex. Where mice from both sexes were used, sex-disaggregated data for disease development or progression were provided as Supplementary Figure. Randomization was performed for in vivo experiments. Data were analyzed with GraphPad Prism version 9. Data are presented as mean ± standard deviation, individual values as scatter plot with column bar graphs. Boxplots show the distribution of values, with the central line indicating the median, box edges representing the 25th and 75th percentiles, and whiskers extending to the minimum and maximum values. Differences were considered significant when $P < 0.05$. N values represent biological replicates. Survival curves were compared using the log-rank test (Mantel–Cox). All the statistics and reproducibility are reported in the figure legend.

Reporting summary

Further information on research design is available in the Nature Portfolio Reporting Summary linked to this article.

Data availability

Source data are provided for the main figures and extended data figures. The RNA-seq data generated by this study have been deposited in the GEO public repository available at the following link [https://www.ncbi.nlm.nih.gov/geo/query/acc.cgi?acc=GSE306088] under the GSE306088 accession number. Metabolomic data generated by this study are publicly available at the following link: [https://data.mendeley.com/datasets/mtbf64xp7d/1], https://doi.org/10.17632/mtbf64xp7d.1. The microbiome sequences generated by this study have been deposited in the European Nucleotide Archive (ENA) under accession number ERP176925. All data are included in the Supplementary Information or available from the authors, as are unique reagents used in this Article. The raw numbers for charts and graphs are available in the Source Data file whenever possible. Source data are provided in this paper.

Code availability

All original code for the analysis of RNA-seq data has been deposited on GitHub (https://github.com/auroramaurizio/RNAseq_BMDCs_PM_PH) and Zenodo (https://zenodo.org/records/17234616) repositories.

References

1. Malard, F. et al. Multiple myeloma. *Nat. Rev. Dis. Prim.* **10**, 45 (2024).
2. Rajkumar, S. V., Kumar, S., Lonial, S. & Mateos, M. V. Smoldering multiple myeloma current treatment algorithms. *Blood Cancer J.* **12**, 129 (2022).
3. Brevi, A., Cogrossi, L. L., Lorenzoni, M., Mattorre, B. & Bellone, M. The insider: Impact of the gut microbiota on cancer immunity and response to therapies in multiple Myeloma. *Front Immunol.* **13**, 845422 (2022).
4. Chesi, M. et al. AID-dependent activation of a MYC transgene induces multiple myeloma in a conditional mouse model of post-germinal center malignancies. *Cancer Cell* **13**, 167–180 (2008).
5. Calcinotto, A. et al. Modifications of the mouse bone marrow microenvironment favor angiogenesis and correlate with disease progression from asymptomatic to symptomatic multiple myeloma. *Oncoimmunology* **4**, e1008850 (2015).
6. Calcinotto, A. et al. Microbiota-driven interleukin-17-producing cells and eosinophils synergize to accelerate multiple myeloma progression. *Nat. Commun.* **9**, 4832 (2018).
7. Bellone M., Brevi A. & Huber S. Microbiota-propelled T helper 17 cells in inflammatory diseases and cancer. *Microbiol Mol. Biol. Rev.* **84**, https://doi.org/10.1128/mmbr.00064-19 (2020).
8. Routy, B. et al. The gut microbiota influences anticancer immunosurveillance and general health. *Nat. Rev. Clin. Oncol.* **15**, 382–396 (2018).
9. Costa, F., Das, R., Kini Bailur, J., Dhodapkar, K. & Dhodapkar, M. V. Checkpoint inhibition in myeloma: Opportunities and challenges. *Front. Immunol.* **9**, 2204 (2018).
10. Termini, R. et al. Circulating tumor and immune cells for minimally invasive risk stratification of smoldering multiple myeloma. *Clin. Cancer Res.* **28**, 4771–4781 (2022).
11. Lesokhin, A. M., Bal, S. & Badros, A. Z. Lessons learned from checkpoint blockade targeting PD-1 in multiple myeloma. *Cancer Immunol. Res* **7**, 1224–1229 (2019).
12. Ishibashi, M. et al. Myeloma drug resistance induced by binding of myeloma B7-H1 (PD-L1) to PD-1. *Cancer Immunol. Res* **4**, 779–788 (2016).
13. McCulloch, J. A. et al. Intestinal microbiota signatures of clinical response and immune-related adverse events in melanoma patients treated with anti-PD-1. *Nat. Med* **28**, 545–556 (2022).
14. Hu, Z. I. et al. Immune checkpoint inhibitors unleash pathogenic immune responses against the microbiota. *Proc. Natl Acad. Sci. USA* **119**, e2200348119 (2022).
15. Johnson, D. et al. IL17A Blockade successfully treated psoriasiform dermatologic toxicity from immunotherapy. *Cancer Immunol. Res.* **7**, 860–865 (2019).
16. Maura, F. et al. The genomic landscape of Vk*MYC myeloma highlights shared pathways of transformation between mice and humans. *Nat. Commun.* **15**, 3844 (2024).

17. Yousef, S. et al. Immunomodulatory molecule PD-L1 is expressed on malignant plasma cells and myeloma-propagating pre-plasma cells in the bone marrow of multiple myeloma patients. *Blood Cancer J.* **5**, e285 (2015).
18. Chesi, M. et al. Drug response in a genetically engineered mouse model of multiple myeloma is predictive of clinical efficacy. *Blood* **120**, 376–385 (2012).
19. Moos, S., Mohebiany, A. N., Waisman, A. & Kurschus, F. C. Imiquimod-induced psoriasis in mice depends on the IL-17 signaling of keratinocytes. *J. Invest Dermatol* **139**, 1110–1117 (2019).
20. Imai, Y. et al. Cutting Edge: PD-1 regulates imiquimod-induced psoriasiform dermatitis through inhibition of IL-17A expression by innate gammadelta-low T cells. *J. Immunol.* **195**, 421–425 (2015).
21. Ghoreschi, K. et al. Generation of pathogenic T(H)17 cells in the absence of TGF-beta signalling. *Nature* **467**, 967–971 (2010).
22. Barnden, M. J., Allison, J., Heath, W. R. & Carbone, F. R. Defective TCR expression in transgenic mice constructed using cDNA-based alpha- and beta-chain genes under the control of heterologous regulatory elements. *Immunol. Cell Biol.* **76**, 34–40 (1998).
23. Bosteels, V. et al. LXR signaling controls homeostatic dendritic cell maturation. *Sci. Immunol.* **8**, eadd3955 (2023).
24. De Filippis, F. et al. High-level adherence to a Mediterranean diet beneficially impacts the gut microbiota and associated metabolome. *Gut* **65**, 1812–1821 (2016).
25. Rodriguez-Garcia, A. et al. Short-chain fatty acid production by gut microbiota Oredicts Treatment Response in Multiple Myeloma. *Clin. Cancer Res.* **30**, 904–917 (2024).
26. Rooks, M. G. & Garrett, W. S. Gut microbiota, metabolites and host immunity. *Nat. Rev. Immunol.* **16**, 341–352 (2016).
27. Culp, E. J. & Goodman, A. L. Cross-feeding in the gut microbiome: Ecology and mechanisms. *Cell Host Microbe* **31**, 485–499 (2023).
28. Abdugheni, R. et al. Metabolite profiling of human-originated Lachnospiraceae at the strain level. *Imeta* **1**, e58 (2022).
29. Shah, U. A. et al. Sustained minimal residual disease negativity in multiple myeloma is associated with stool -butyrate and healthier plant-based fiets. *Clin. Cancer Res.* **28**, 5149–5155 (2022).
30. Bachem, A. et al. Microbiota-derived short-chain fatty acids promote the memory potential of antigen-activated CD8(+) T cells. *Immunity* **51**, 285–297 (2019).
31. Nomura, M. et al. Association of short-chain fatty acids in the gut microbiome with clinical response to treatment with nivolumab or pembrolizumab in patients with solid cancer tumors. *JAMA Netw. Open* **3**, e202895 (2020).
32. Miller, K. D. et al. Acetate acts as a metabolic immunomodulator by bolstering T-cell effector function and potentiating antitumor immunity in breast cancer. *Nat. Cancer* **4**, 1491–1507 (2023).
33. Richard, S. et al. Clinical response and pathway-specific correlates following TIGIT-LAG3 blockade in myeloma: the MyCheckpoint randomized clinical trial. *Nat. Cancer* **5**, 1459–1464 (2024).
34. Simpson, R. C., Shanahan, E. R., Scolyer, R. A. & Long, G. V. Towards modulating the gut microbiota to enhance the efficacy of immune-checkpoint inhibitors. *Nat. Rev. Clin. Oncol.* **20**, 697–715 (2023).
35. Routy, B. et al. Fecal microbiota transplantation plus anti-PD-1 immunotherapy in advanced melanoma: a phase I trial. *Nat. Med.* **29**, 2121–2132 (2023).
36. Wang, Y. et al. Fecal microbiota transplantation for refractory immune checkpoint inhibitor-associated colitis. *Nat. Med.* **24**, 1804–1808 (2018).
37. Porcari, S. et al. Key determinants of success in fecal microbiota transplantation: From microbiome to clinic. *Cell Host Microbe* **31**, 712–733 (2023).
38. Bender, M. J. et al. Dietary tryptophan metabolite released by intratumoral Lactobacillus reuteri facilitates immune checkpoint inhibitor treatment. *Cell* **186**, 1846–1862 (2023).
39. Lee, S. H. et al. Bifidobacterium bifidum strains synergize with immune checkpoint inhibitors to reduce tumour burden in mice. *Nat. Microbiol.* **6**, 277–288 (2021).
40. Arellano, M. et al. Routine analysis of short-chain fatty acids for anaerobic bacteria identification using capillary electrophoresis and indirect ultraviolet detection. *J. Chromatogr. B Biomed. Sci. Appl.* **741**, 89–100 (2000).
41. Jian, X. et al. Alterations of gut microbiome accelerate multiple myeloma progression by increasing the relative abundances of nitrogen-recycling bacteria. *Microbiome* **8**, 74 (2020).
42. Zhu, Y. et al. Targeting gut microbial nitrogen recycling and cellular uptake of ammonium to improve bortezomib resistance in multiple myeloma. *Cell Metab.* **36**, 159–175.e158 (2024).
43. Wang, B., Morinobu, A., Horiuchi, M., Liu, J. & Kumagai, S. Butyrate inhibits functional differentiation of human monocyte-derived dendritic cells. *Cell Immunol.* **253**, 54–58 (2008).
44. Shah, U. A., Parikh, R., Castro, F., Bellone, M. & Lesokhin, A. M. Dietary and microbiome evidence in multiple myeloma and other plasma cell disorders. *Leukemia* **37**, 964–980 (2023).
45. Pianko, M. J. et al. Minimal residual disease negativity in multiple myeloma is associated with intestinal microbiota composition. *Blood Adv.* **3**, 2040–2044 (2019).
46. Giuliani, N., Rizzoli, V. & Roodman, G. D. Multiple myeloma bone disease: Pathophysiology of osteoblast inhibition. *Blood* **108**, 3992–3996 (2006).
47. Sato, K. et al. Th17 functions as an osteoclastogenic helper T cell subset that links T cell activation and bone destruction. *J. Exp. Med.* **203**, 2673–2682 (2006).
48. Tyagi, A. M. et al. The microbial metabolite butyrate stimulates bone formation via T regulatory cell-mediated regulation of WNT10B expression. *Immunity* **49**, 1116–1131.e1117 (2018).
49. Liu, C. et al. Blocking IL-17A enhances tumor response to anti-PD-1 immunotherapy in microsatellite stable colorectal cancer. *J. Immunother. Cancer* **9**, https://doi.org/10.1136/jitc-2020-001895 (2021).
50. Varaljai, R. et al. Interleukin 17 signaling supports clinical benefit of dual CTLA-4 and PD-1 checkpoint inhibition in melanoma. *Nat. Cancer* **4**, 1292–1308 (2023).
51. Coutzac, C. et al. Systemic short chain fatty acids limit antitumor effect of CTLA-4 blockade in hosts with cancer. *Nat. Commun.* **11**, 2168 (2020).
52. Anderson, R., Theron, A. J. & Rapoport, B. L. Immunopathogenesis of immune checkpoint inhibitor-related adverse events: roles of the intestinal microbiome and Th17 cells. *Front. Immunol.* **10**, 2254 (2019).
53. Esfahani, K. & Miller, W. H. Jr. Reversal of autoimmune toxicity and loss of Tumor Response by Interleukin-17 Blockade. *N. Engl. J. Med.* **376**, 1989–1991 (2017).
54. Lechner, M. G. et al. Inhibition of IL-17A protects against thyroid immune-related adverse events while preserving checkpoint inhibitor antitumor efficacy. *J. Immunol.* **209**, 696–709 (2022).
55. Wang, F., Yin, Q., Chen, L. & Davis, M. M. Bifidobacterium can mitigate intestinal immunopathology in the context of CTLA-4 blockade. *Proc. Natl. Acad. Sci. USA* **115**, 157–161 (2018).
56. De Filippis, F. P. et al. D. Distinct genetic and functional traits of human intestinal prevotella copri strains are associated with different habitual diets. *Cell Host Microbe* **13**, 444–453 (2019).
57. Prasoodanan, P. K. V. S. et al. V. K. Western and non-western gut microbiomes reveal new roles of Prevotella in carbohydrate metabolism and mouth–gut axis. *NPJ Biofilms Microbiomes* **7**, 1–17 (2021).
58. Jean-Pierre, F. et al. Community composition shapes microbial-specific phenotypes in a cystic fibrosis polymicrobial model system. *Elife* **12**, https://doi.org/10.7554/elife.81604 (2023).

59. Qudeimat, M. A., Alyahya, A., Karched, M., Behbehani, J. & Salako, N. O. Dental plaque microbiota profiles of children with caries-free and caries-active dentition. *J. Dent.* **104**, 103539 (2021).
60. Wen, C. et al. Quantitative metagenomics reveals unique gut microbiome biomarkers in ankylosing spondylitis. *Genome Biol.* **18**, 142 (2017).
61. Wang, S. et al. Bile acid-microbiome interaction promotes gastric carcinogenesis. *Adv. Sci.* **9**, e2200263 (2022).
62. Yang, D. et al. Dysregulated lung commensal bacteria drive interleukin-17B production to promote pulmonary fibrosis through their outer membrane vesicles. *Immunity* **50**, 692–706 (2019).
63. Mangalam, A. et al. Human gut-derived commensal bacteria suppress CNS inflammatory and demyelinating disease. *Cell Rep.* **20**, 1269–1277 (2017).
64. Griffin, M. E. E. et al. Enterococcus peptidoglycan remodeling promotes checkpoint inhibitor cancer immunotherapy. *Science* **373**, 1040–1046 (2021).
65. Cao WZ, C. et al. Clostridium butyricum potentially improves inflammation and immunity through alteration of the microbiota and metabolism of gastric cancer patients after gastrectomy. *Front. Immunol.* **13**, 1–14 (2022).
66. Lin, B. et al. Randomized clinical trial: probiotics alleviated oral-gut microbiota dysbiosis and thyroid hormone withdrawal-related complications in thyroid cancer patients before radioiodine therapy following thyroidectomy. *Front. Endocrinol.* **13**, 1–15 (2022).
67. Nakae, S. et al. Antigen-specific T cell sensitization is impaired in IL-17-deficient mice, causing suppression of allergic cellular and humoral responses. *Immunity* **17**, 375–387 (2002).
68. Affer, M. et al. Promiscuous MYC locus rearrangements hijack enhancers but mostly super-enhancers to dysregulate MYC expression in multiple myeloma. *Leukemia* **28**, 1725–1735 (2014).
69. Love, M. I., Huber, W. & Anders, S. Moderated estimation of fold change and dispersion for RNA-seq data with DESeq2. *Genome Biol.* **15**, 550 (2014).
70. Yu, G., Wang, L. G., Han, Y. & He, Q. Y. clusterProfiler: an R package for comparing biological themes among gene clusters. *OMICS* **16**, 284–287 (2012).

Acknowledgements

This work was supported by Blood Cancer United, formerly The Leukemia & Lymphoma Society (Grant #6618-21 to M.B.) and the Cancer Research Institute (CLIP Grant #CRI4838 to M.B.). The research leading to these results has also received funding from AIRC under IG 2018 - ID. 21808 project – P.I. M.B. L.L.C. conducted this study in partial fulfillment of her Ph.D. at San Raffaele University. We thank the International Myeloma Society (IMS) for the IMS Young Investigation Award to L.L.C. We thank Dr. Arianna Brevi for the initial experimental training. We thank Dr. Valeria Mannella from Proteomics and Metabolomics Facility (ProMeFa; IRCCS Ospedale San Raffaele). We thank Dr. Amleto Fiocchi from the Animal Histopathology facility (IRCCS Ospedale San Raffaele and Universita Vita-Salute San Raffaele). We thank Dr Yoichiro Iwakura (Institute of Medical Science, Tokio, Japan) for providing us IL-17KO mice.

Author contributions

M.B. and L.L.C. designed and conceived the study. L.L.C. performed most of the experiments and analyzed data. A.Po. performed some in vivo and in vitro experiments. P.Z. and B.M. performed in vitro experiments with human cells. M.G. helped with in vivo experiments and maintained the murine colonies. M.L. and G.M. helped with some in vivo experiments. N.R. and F.S. performed histological evaluation and scoring. S.S. and N.C. provided and maintained bacterial cultures, performed and analyzed microbiome sequencing data. A.T. and A.R. performed and analyzed Multiplex IHC. A.Pa. and C.A. performed and analyzed NMR experiments. A.M. performed bioinformatic analysis of RNASeq. M.C. and L.B. provided genetically engineered mice. L.L.C. prepared the figures and tables. M.B. and L.L.C. wrote the manuscript. All authors contributed to critically reading the manuscript and approved the final version.

Competing interests

M.B. is co-owner of the patent EP18209623.0, "Strategies to improve colonization and expression of *Prevotella melaninogenica* in the gut of patients affected by IL-17-mediated diseases". M.C. reports grants from NCI during the conduct of the study; grants from Pfizer and nonfinancial support from BMS outside the submitted work; in addition, M.C. has a patent for hCRBN transgenic mice licensed to Novartis and a patent for VkMYC cell line licensed to Pfizer. P.L.B. reports personal fees from CellCentric, grants from NCI, Myeloma Solutions Fund and Paula and Rodger Riney Foundation during the conduct of the study; personal fees from Pfizer, AbbVie, Salarius, Oncopeptides, and GlaxoSmithKline outside the submitted work; in addition, P.L.B. has a patent for hCRBN transgenic mice licensed to Novartis and a patent for VkMYC cell line licensed to Pfizer. All other authors have no competing interests.

Additional information

Supplementary information The online version contains supplementary material available at https://doi.org/10.1038/s41467-025-65312-y.

Correspondence and requests for materials should be addressed to Matteo Bellone.

Peer review information *Nature Communications* thanks María Linares and the other anonymous reviewer(s) for their contribution to the peer review of this work. A peer review file is available.